Front. Optoelectron. 2020, 13(2): 156–187
https://doi.org/10.1007/s12200-020-1003-5

REVIEW ARTICLE

Recent advances, challenges, and opportunities of inorganic nanoscintillators

Santosh K. GUPTA[1], Yuanbing MAO (✉)[2]

1 Radiochemistry Division, Bhabha Atomic Research Centre, Trombay, Mumbai 400085, India
2 Department of Chemistry, Illinois Institute of Technology, Chicago, IL 60616, USA

Abstract This review article highlights the exploration of inorganic nanoscintillators for various scientific and technological applications in the fields of radiation detection, bioimaging, and medical theranostics. Various aspects of nanoscintillators pertaining to their fundamental principles, mechanism, structure, applications are briefly discussed. The mechanisms of inorganic nanoscintillators are explained based on the fundamental principles, instrumentation involved, and associated physical and chemical phenomena, etc. Subsequently, the promise of nanoscintillators over the existing single-crystal scintillators and other types of scintillators is presented, enabling their development for multifunctional applications. The processes governing the scintillation mechanisms in nanodomains, such as surface, structure, quantum, and dielectric confinement, are explained to reveal the underlying nanoscale scintillation phenomena. Additionally, suitable examples are provided to explain these processes based on the published data. Furthermore, we attempt to explain the different types of inorganic nanoscintillators in terms of the powder nanoparticles, thin films, nanoceramics, and glasses to ensure that the effect of nanoscience in different nanoscintillator domains can be appreciated. The limitations of nanoscintillators are also highlighted in this review article. The advantages of nanostructured scintillators, including their property-driven applications, are also explained. This review article presents the considerable application potential of nanostructured scintillators with respect to important aspects as well as their physical and application significance in a concise manner.

Keywords scintillators, nanoscintillators, inorganic, photoluminescence, radioluminescence

Received January 8, 2020; accepted March 19, 2020

E-mail: ymao17@iit.edu

1 Introduction

1.1 Scintillation mechanism

Scintillators are classified as a type of luminescent materials that have great potentials to detect ionizing radiations such as X-rays, γ-rays, β-rays, and neutrons. Further, they serve as an energy transformer, i.e., they convert high-energy X-rays or γ-rays into lower-energy ultraviolet (UV) and visible (Vis) lights (400–700 nm). Therefore, these materials are applicable in areas of considerable scientific and technological importance, such as photodynamic therapy [1], security [2], well logging [3], and medical imaging [4]. Scintillators include two important components: scintillating materials and photodetectors (PDs). PDs convert the generated UV–Vis light into detectable and measurable electrical signals. Figure 1 shows the instrumental setup involved in the scintillation process.

The scintillation process occurs when the UV or Vis light is emitted after exposure to highly energetic ionizing radiation. The performance of scintillation materials is mainly dependent on their luminosity, the lifetime of the excited state, and the emission maxima (λ_{max}) [5]. Other important characteristics of scintillator materials include their ruggedness, radiation stability, thermal stability, chemical stability, and mechanical strength. These characteristics determine the optimum performance and possible applications of a scintillator material. Its light conversion efficiency (η_{scin}) relies on the following three processes: conversion (β), transfer (Q), and luminescence (S). These three processes are related by Eq. (1), where

$$\eta_{scin} = \beta SQ, \tag{1}$$

where β is the phenomenological parameter (2–3 in case of most scintillators) [6]. One of the oldest and best inorganic scintillator materials is silver-activated zinc sulfide (ZnS: Ag), the efficiency of which is much higher than that of

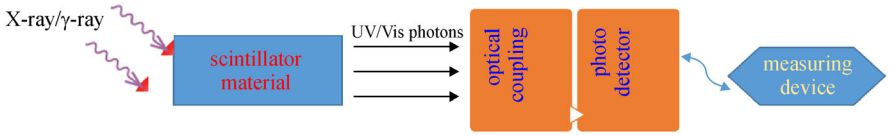

Fig. 1 Instrumental setup involved in the scintillation process

NaI(Tl) [7]. However, its usage is limited only to alpha particles and heavy-ion detection because it is available only in a polycrystalline form and its usability is limited to thin screens [8]. Therefore, scientists have been searching for materials with improved scintillation performance and better efficiency. Research efforts along these directions are in full swing globally, mostly focusing on the X-ray imaging applications. Scintillation involves three basic processes, i.e., absorption, migration, and emission as shown in Fig. 2.

Absorption is the process during which highly energetic ionizing radiation, namely X-rays or γ-rays, is absorbed by the scintillation crystals or powders to form e^-–h^+ pairs (exciton), which can freely move inside the defect states depending upon their momentum. Migration is the process during which excitons are transported through the lattice of the scintillating media. During this process, some excitons are nonradiatively lost via recombination at the quenching centers, which reduces the number of exciton pairs actually available for achieving radiative luminescence or the actual scintillation process. Only the excitons, which have sufficient momentum and kinetic energy, reach the luminescent centers and contribute to scintillation. The efficiency of this process is given by the parameter S. The remaining e^-–h^+ pairs radiatively recombine and cause the scintillating emission of Vis or UV photons. The intrinsic efficiency of radiative recombination at the luminescent center is quantified by Q.

The overall conversion efficiency (from high-energy to low-energy photons) is given by the number of photons $N_{e/h}$ produced per energy of the incoming particle (Eq. (2)), where

$$N_{e/h} = \frac{E_{\text{inc}}}{\beta E_{\text{g}}} SQ, \tag{2}$$

where E_{inc} is incident energy, $N_{e/h}$, S, and Q are the number of electron–hole pairs generated during the multiplication stage, the efficiency with which the luminescent centers are excited by the energy carriers, and the quantum efficiency of the luminescent center, respectively. The average quantum efficiency (Q) over the emission spectrum of a typical scintillator is approximately 15%–20%, and the maximum quantum efficiency is 25%–30%. The average energy E required to generate an exciton is considerably higher than that of the exciton itself, i.e., $E = \beta E_{\text{g}}$ $(\beta > 1)$. Shockley approximation postulated that the average energy required to generate an $e^- - h^+$ pair is $E = 3E_{\text{g}}$, where E_{g} is the bandgap of a host lattice [10]. Robbins observed that the average energy required for creating an exciton pair is $(2.3E_{\text{g}} - 7E_{\text{g}})$, depending on the type of host lattice [11]. Higher values are observed for lattices with higher vibrational frequencies.

1.2 Inorganic scintillators

The very first scintillator material, i.e., NaI(Tl), was discovered in 1948. Subsequently, there has been growing

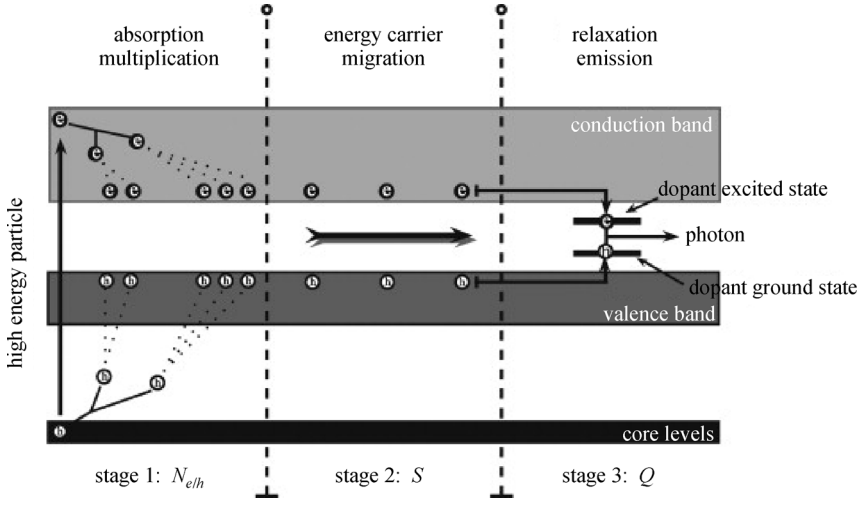

Fig. 2 Schematic depicting the various stages involved in scintillation [9]. Copyright 2010. Reproduced with permission from Elsevier

interest in the exploration of new types of scintillators for various applications. Until now, scientists have reported several types of scintillators such as alkali, alkaline earth, and rare earth (RE) halides, including NaI:Tl, LiI:Eu, BaF_2:Ce, CaF_2:Eu, CeF_3, and $LaBr_3$:Ce [12–18]. Unfortunately, these materials have many shortcomings such as their hygroscopic nature that limits their practical applications. An ideal scintillator should exhibit various features, including (i) a high effective atomic number (Z), (ii) a high photon output or light yield (LY, low-energy photons produced per unit energy deposited, photons/MeV), (iii) a short emission decay lifetime, (iv) low synthesis cost, (v) easy scalability, and (vi) high density [19].

Depending on the nature of the host materials, scintillators are categorized as organic scintillators, inorganic scintillators, and gaseous scintillators [20]. This review article focuses on inorganic scintillators, we have provided sub-classifications of nanoscintillators under inorganic scintillators with a brief overview.

Unlike organic scintillators (OSs), the scintillation mechanism of inorganic scintillators (ISs) is dependent on the nature and crystal structure of the host lattice (HL). Hosts are mostly single crystals, which are doped with a small number of activator ions as impurities, absorb holes and electrons, and produce luminescence. They can also be semi-crystalline and amorphous such as ceramics and glasses. High temperature is usually needed for growing crystals of ISs such as alkali metal halides [21]. In ISs, luminescence originates from the bulk property of materials, whereas individual molecules contribute to the scintillation process in OSs. The scintillation mechanism of inorganic crystals is presented in Fig. 3(a) [22]. Electrons normally occupy only the selected energy levels in a pure inorganic crystal lattice such as NaI or ZnS. In case of pure crystals, electrons can never be observed in its bandgap. The absorption of external energy can only excite electrons from the valence band (VB) to the conduction band (CB), resulting in a hole in the VB. However, photon emission is not an efficient process for an electron to reoccupy the VB. Per decay, only few photons are released, whereas energy is emitted by several mechanisms. In addition, the bandgap widths of pure crystals are high, and the resulting emitted photon is not within the visible range. Therefore, small amounts of activator ions are added to these crystals to shift the emitted photons to the visible region. Thus, the energy level diagram is modified by creating intermediate states in the bandgap of HL. Such modifications do not alter the energy levels of HL but change the energy structure at the activator sites. The typical emission spectra of undoped and Tl- and Na-doped CsI crystals are shown in Fig. 3(b).

The common ISs include alkali halides (NaI) doped with Tl and ZnS doped with Cu, Ag, or Mn. Most of the inorganic glasses are formed from the oxides of the Si, B, P, or Li ions. NaI(Tl) and CsI(Na) (high light output) are normally used in case of high-resolution γ-ray spectroscopy. In addition, other types of ISs exist with unique properties for specific applications [23]. NaI(Tl) is widely explored in general scintillation counting, health physics, environmental monitoring, and high-temperature applications. On the other hand, CsI(Tl) is extensively employed for particle and high-energy physics research, general radiation detection, photodiode readout, and photoswitching. $CeBr_3$ exhibits exceptional light emission and a fast light de-excitation time; it is frequently used in particle and high-energy physics as well as high-resolution spectroscopy. In high-energy physics applications, the use of bismuth germanate ($Bi_4Ge_3O_{12}$; BGO) crystals (high density and Z) improve the γ-ray energy confinement. BGO is widely used in geophysical research, positron emission tomography (PET), and anti-Compton spectrometers. $LaBr_3$ with improved energy resolution and good linearity in a wide temperature range is widely used in homeland security.

The advantage of ISs over OSs is their high specific energy loss (dE/dx) because of the higher density and atomic number of HL. In addition, undoped ISs have been used for achieving defect-induced scintillation in pure

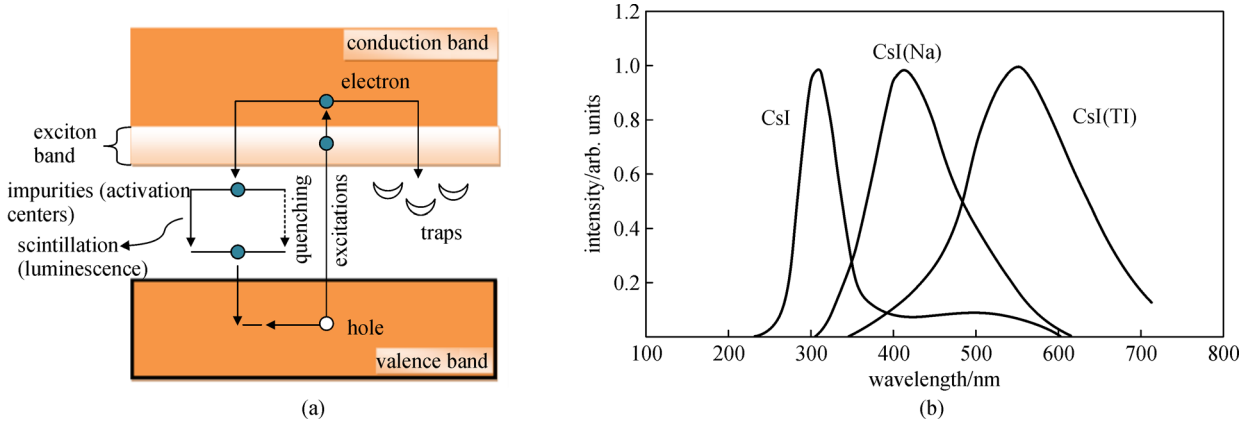

Fig. 3 (a) Mechanism of scintillation in inorganic crystals and (b) emission spectra of three typical inorganic scintillators with and without activators [22]. Copyright 2013. Reproduced with permission from Springer

compounds such as yttrium aluminum garnet (YAG), $PbWO_4$, and $CaWO_4$ [24–26]. The radioluminescence (RL) in pure crystals is mostly associated with the excitons localized near the defects due to the deviation from their stoichiometric composition [27]. The emission profile from the defect-induced RL has a broad spectral band, limiting its color purity and commercial viability.

ISs can be further classified as bulk single crystals (BSCs), bulk microcrystalline scintillators (BMSs), and nanocrystalline scintillators (NCSs). Recently, other novel classes of materials have been added to the category of NCSs such as nanoclusters, metal organic frameworks (MOFs), quantum dots (QDs), and nanophosphors [28–32]. The scintillation mechanism, which governs NCSs, is similar to those of normal ISs and BSCs. However, differences may be observed because of defect density and the availability of the effective energy states to electrons. Our research group has worked extensively on the exploitation of NCSs, particularly with respect to doped pyrochlore nanoparticles (NPs), including $La_2Zr_2O_7$, $La_2Hf_2O_7$, $Gd_2Hf_2O_7$, and $Y_2Hf_2O_7$, which are considered to be excellent photo- and radioluminescence hosts [33–50]. NCSs have a high surface-to-volume ratio that allows a high extent of surface modulation and multivalent binding capability, resulting in high specificity. ZnSe is another promising inorganic scintillator. Jagtap et al. discussed the scintillation performance of the ZnSe-based scintillators and ZnSe quantum dots as well as the advantages of the ZnSe QD scintillators [51].

Recently, perovskite-based scintillators have attracted significant attention from the scientific community. These scintillators include halide perovskite bulk films or nanocrystals, denoting short decay time and strong X-ray absorption [52–54]. Moreover, emerging lead-free perovskites with considerable LY have drawn immense interest in the field of optoelectronics [55,56].

1.3 Scintillation at the nanoscale

1.3.1 Background

Recently, many research efforts are targeted toward the design of novel and highly efficient scintillators for the detection of ionizing radiation and imaging for medical diagnostics [57–62]. Some of the examples of BSCs include NaI:Tl, CsI:Tl, $Bi_4Ge_3O_{12}$ (BGO), $BaF_2:Ce^{3+}$, $Y_3Al_5O_{12}:Ce^{3+}$ (YAG:Ce^{3+}), lithium molybdate, YAG:Yb, and $Tl_2GdCl_5:Ce^{3+}$ [63–68]. BSCs are normally required to detect strongly ionizing radiation because high optical transmission in a particular emission range is needed for a scintillator to emit efficiently [69]. The high optical transparency offered by BSCs has huge advantages for the detection of ionizing radiation. Their large size and high energy resolution make them suitable for various applications, particularly for nuclear imaging, gamma probe, well counting, X-ray imaging, and radioluminescence microscopy [70].

As depicted in Fig. 1, the scintillation process of BSCs requires their coupling with detectors, usually photomultiplier tube (PMT), to achieve the quantification of emitting photons. Most of the work on scintillation is related to visible photon emission that can be easily detected by PMT. Few issues are associated with BSCs because the single-crystal growth of BSCs is highly cost-intensive and requires ultra-pure chemicals, highly sophisticated instrumentation, and long processing time (as long as six months) [13,65,71–74].

Flexibility and scalability are the most common issues in γ-ray detection using BSCs. For example, a high-purity germanium detector (HPGe) has a very high energy resolution (0.2% energy resolution at 1.33 MeV). It needs liquid nitrogen (77 K) for day-to-day operation eliminate thermal noise [75,76]. However, cadmium–zinc–telluride (CZT) works efficiently at room temperature (1% at 662 keV), but its crystal growth is limited to a few centimeters in each direction [77]. Finally, the most commonly used scintillator, i.e., Tl-doped sodium iodide (NaI), can be grown as large crystals; however, it has a low energy resolution (7% energy resolution at 662 keV) [78].

To improve the scintillator efficiency, depending upon the emission requirement, large BSCs having a good atomic structure and doped with suitable activators are required. However, the currently used BSCs have several limitations such as expensive synthesis, long processing time, low energy resolution, and chemical instability, which restrict their usability [79,80]. Over the past decade, research on nanoscintillators has gained attention because of promising results, which has sparked an ongoing debate whether designing BSCs is the only way to improve scintillation.

BMSs are a less costly alternative to traditionally used BSCs. However, compacting BMSs is a huge challenge due to the large number of pores present inside them, which cause scattering of light and low optical transparency [81]. Thus, their usage is restricted to conventional screens and photostimulable storage screens for medical radiography [81,82]. In addition, BMSs have low miscibility in polymers and gels, making them commercially less viable. On the other hand, bulk OSs are much more compatible with the polymeric matrix even though they are not applicable as neutron scintillators because of their incompatibility with $^6Li_3$ [83]. Because of these limitations of BSCs, BMSs, and bulk OSs, NCSs have been in high demand in recent years.

One dimension of NCSs is 1–100 nm. Consequently, they have high aspect (l/d) and surface-to-volume (S/V) ratios, resulting in their high reactivity. Recently, increasing attention has been devoted to the nanocrystalline powder scintillators such as doped alkaline earth chalcogenides, doped aluminum garnets (YAG and LuAG), and BGO [5,59,60,84–86]. They have several advantages over

BSCs, such as high stopping power, self-activated luminescence, and feasibility in transparent nanoceramics or nanocomposites. Furthermore, because of the relative dominance of the surface atoms on NPs, their properties, particularly optical properties, can be easily tuned due to the better e^{-}–h^{+} overlap integral. Their performance as scintillators is considerably dependent on the manner in which RL can be controlled and the manner in which the transport process occurs at multiple length scales (nano → micro → meso). For example, Stouwdam and van Veggel and Kömpe et al. observed a substantial increase in the quantum efficiency (QE) of the rare-earth-ion-doped nanophosphors on modifying the surface of the NPs [87,88]. On the other hand, Cooke et al. observed an enhancement in τ_{lumin} in case of Y_2SiO_5:Ce NPs when compared with those of their bulk counterparts [89,90].

In case of X-ray imaging detectors, the QE of Gd_2O_3:Eu NCSs was considerably lower than those of BMSs because of quenching by the large density of surface defects and the disorder around the dopant ions in NCSs [91]. There are a few reports in which NCSs have shown improved scintillation efficiency when compared with those of BSCs and BMSs. For example, the YAG:Eu nanopowder showed improved QE compared to its BSCs by a factor of 4 [82]. Also, the rise time decreased in nanocrystalline borate when compared with that in its single-crystal counterpart [92]. Other than being used for imaging screens in X-ray radiography, NCSs have several other important medical applications in X-ray-induced photodynamic therapy (XPDT), bioimaging, and cell labeling [70,82,93,94]. Jung et al. compiled various NCSs and BSCs based on their RL efficiency [82].

Although plenty of research has been conducted on luminescent NPs by focusing on their lighting and display applications, their exploration as scintillators is still in its initial stage. NPs present a new realm of opportunities in case of scintillation technologies, and this review article presents a preliminary investigation of the scintillation response of nanomaterials. Moreover, this review article denotes the basic physical properties that govern scintillation at the nanosized and bulk levels and the chemical compositions of the ISs as well as their types. This review article also presents the suitability of nanostructured and bulk scintillators for specific applications along with their advantages and disadvantages. We have also presented applications specific to nanostructured and bulk scintillators. The detection capabilities of the photon-counting and energy integration detectors are discussed along with their advantages and disadvantages. Finally, we summarize all the results, providing ample information about the future perspective of the current topic.

1.3.2 Advantages and disadvantages of NCSs

The nanocomposites designed by dispersing high-Z NPs, such as HfO_2 and BaF_2, and dyes in a polymer matrix are expected to improve the scintillation efficiency because of the high Z of the inorganic materials and fast decay owing to polymers [19,95]. Such nanocomposite-based scintillators reduce the cost due to the low cost of plastics. Moreover, they allow easily tunable spectral properties, such as energy range and resolution, enabling isotope identification. It is much easier and cheaper to synthesize nanocomposites when compared with large single crystals. A 60% increase in PL QE was reported in case of the silicon nanocrystals encapsulated inside a tightly packed matrix [96].

Because of the large surface area of the NPs, the traditional mixing techniques cause considerable agglomeration and phase segregation. This adversely affects the uniformity and transparency of the prepared nanocomposites [97]. Therefore, high NP loading in the polymer matrix is a challenge, limiting its application in various technological areas [98]. Several strategies, such as surface coatings/modification and *in situ* NP formation, have been employed to address this issue. However, designing bulk nanocomposites with high NP loading and optimum transparency is still an issue [99,100]. High-temperature compaction has usually been applied to obtain optically transparent nanoscintillators; however, because it increases the particle size, the advantages provided by the NPs are lost. Another problem associated with nanostructured materials is their high surface area and large number of surface defects such as dangling bonds and adsorbed species. These surface defects provide nonradiative pathways to quench the radiative emission of light, which adversely affects the LY of NCSs compared to that obtained in BSCs/BMSs [101].

1.3.3 Suitability of nanostructured scintillators for various applications

The size of crystalline materials plays a very important role in determining their applications [86]. For example, efficient γ-ray detection requires the localization of the γ-ray interaction position in a three-dimensional (3D) manner to a small voxel within a large bulk-crystal-based detector [102]. This manipulation is difficult to achieve in nanocrystals because it requires position-sensitive PMTs that are coupled with bulk crystals [103].

In most cases, γ- and X-ray identification and detection are mainly governed by semiconductor-based detectors, such as high-purity germanium (HPGe) and CdZnTe (CZT), and scintillators, such as NaI:Tl. Substantial effort has been devoted in these fields for improving the detection efficiency; however, these approaches lack spectroscopic utility.

It is postulated that low-cost and large-sized materials with good energy resolution are desirable for γ-ray and neutron detection applications. Scintillators have an advantage over semiconductor detectors in terms of the ease of operation at room temperature and large-scale

production; however, they have lower energy resolution. On the other hand, BSC scintillators have improved radiation detection capability and can outperform polycrystalline materials, glasses, and ceramic-based scintillators. SrI_2:Eu and $LaBr_3$:Ce are highly promising for γ-ray detection. However, their large-scale production is expensive; therefore, replacing the NaI:Tl scintillator remains a challenge.

NSCs have many advantages over BSCs, particularly in case of imaging applications. The spatial resolution of BSCs/BMSs is limited by the spread of light in the scintillation layer. When the microstructured layers are converted into densely and orderly packed thin and long needles or wires, which are coupled to position-sensitive detectors, they are expected to have improved spatial resolution [104]. Taheri et al. extensively studied ZnO nanowires and observed that their spatial resolution is suited to X-ray-based imaging [105,106]. The improved spatial resolution can be attributed to the fact that each individual nanowire acts as an individual light guide, restricting the spread of the optical photons generated inside the imager. Recently, Ashworth tuned the color emission properties of nanocrystals by bandgap tailoring, denoting the possibility of multicolor X-ray scintillation [107].

In case of low-energy XPDT (~300 keV), NCSs are highly favorable. This is mainly because the side effects of radiotherapy can be eliminated in the energy range of 6–20 MeV [108]. Table 1 lists the RL intensity of various NCSs and BSCs.

2 Important characteristics governing the properties of the nanoscintillators

Some important parameters, which are critical with respect to the scintillator performance, are discussed below.

2.1 Structural effect

The structure, size, and nature of NPs play important roles with respect to the design of nanoscintillators with high

Table 1 Comparison of the RL intensity of NCSs and BSCs [82]. Copyright 2014. Reproduced with permission from Elsevier

	nanocrystalline@50-keV X-rays				single crystal@662-keV γ-rays		
sample name (abbreviation)	formula	crystallite size /nm	relative intensity (%BGO) between 300 and 400 nm	relative intensity (%BGO) between 200 and 1000 nm	formula	luminosity (photons/MeV)	relative luminosity (%BGO) between 200 and 1000 nm
BGO	$Bi_4Ge_3O_{12}$	20	100	100	$Bi_4Ge_3O_{12}$	7200	100
					$Y_3Al_5O_{12}$ (undoped)	12190	149
YAG	$Y_3A_{l5}O_{12}$	80	491	30	$Y_3Al_5O_{12}$:Pr (0.08%)	14700	180
YAG:Pr (1%)	$Y_3Al_5O_{12}$:Pr	80	3414	141	$Y_3Al_5O_{12}$:Pr (0.1%)	19440	270
YAG:Pr (0.75%)	$Y_3Al_5O_{12}$:Pr	80	2620	118	$Y_3Al_5O_{12}$:Pr (0.16%)	13770	131
YAG:Pr (1.25%)	$Y_3Al_5O_{12}$:Pr	80	2660	98	$Y_3Al_5O_{12}$:Pr (0.24%)	15500	190
YAG:Pr (1%)@ SiO_2	$Y_3Al_5O_{12}$:Pr@SiO_2	120	855	42	$Y_3Al_5O_{12}$:Pr (0.25%)	16000	222
YAG:Pr (1.5%)	$Y_3Al_5O_{12}$:Pr	90	2960	120	$Y_3Al_5O_{12}$:Pr (0.33%)	15610	216
YAG:Pr (1.75%)	$Y_3Al_5O_{12}$:Pr	90	2620	94	$Y_3Al_5O_{12}$:Pr (0.6%)	11600	140
					$Y_3Al_5O_{12}$:Pr (0.65%)	14670	203
					$Y_3Al_5O_{12}$:Pr (0.8%)	8000	111
LSAO:Pr (0.5%)	(La,Sr)AlO_4:Pr	190	4	9	(La,Sr)AlO_4:Pr	–	–
GSO:Ce (10%)	$Gd_2Si_2O_7$:Ce (10%)	120	782	41	$Gd_2Si_2O_7$:Ce	12500	174
GYGAG:Pr (1%) Gd	$(Gd_{0.7},Y_{0.3})_3(Al_{0.5},Ga_{0.5})_5O_{12}$:Pr (1%)	100	255	116	$(Gd,Y)_3A_5O_{12}$:Pr (1%)	–	–
GYGAG:Pr (1%) Ga	$(Gd_{0.5},Y_{0.5})_3(Al_{0.3},Ga_{0.7})_5O_{12}$:Pr (1%)	100	1220	49	$Y_3(Ga,Al)_5O_{12}$:Pr (1%)	–	–
LYSO:Pr (1%) CR	$(Lu,Y)_2SiO_5$ (1%)	90	350	65	$(Lu,Y)_2SiO_5$:Ce (LYSO)	27000	375
LYSO:Pr (1%) SP	$(Lu,Y)_2SiO_5$ (1%)	20	44	29	$Lu_{1.8}Y_{0.2}SiO_5$:Ce (LYSO)	34000	472
BaF_2	BaF_2	50	78	3	BaF_2 single crystal	3900/10000	54/139

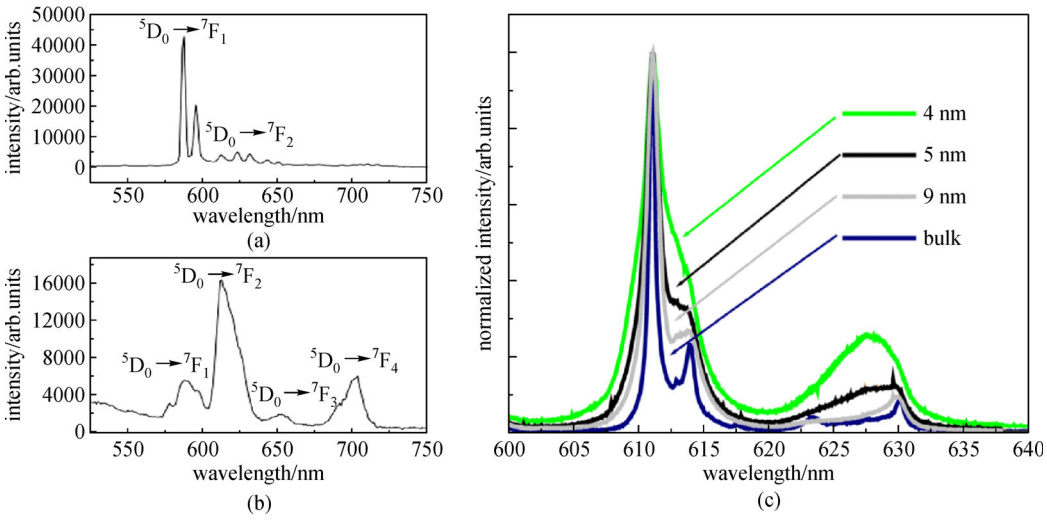

Fig. 4 Emission spectra of the Eu^{3+}-doped (a) bulk and (b) nanosized $Y_2Sn_2O_7$ [110]. Copyright 2013. Reproduced with permission from Elsevier. (c) Emission spectra of the Eu^{3+}-doped bulk and nanosized Gd_2O_3 [101]. Copyright 2010. Reproduced with permission from IEEE

light output and improved performance. The surface strengths induce additional pressure when the size of the materials is reduced to the nanosized regime, causing lattice disorders and significantly affecting the crystal field. This changes the structural parameters of the HL crystals such as the cell constant, unit cell volume, bond length, and bond angle. For example, the metal–oxygen bond length of the Y_2O_3 NPs is different from that of its bulk counterpart [109]. Similarly, the $Y_2Sn_2O_7$ NPs displayed a different structure when compared with their bulk counterpart. These changes may modify the bonding parameters, density of states, and electronic structure [110]. The fluctuation in the crystal field induces Stark splitting of the activator energy levels, which may significantly affect the optical properties of the nanocrystals. Figure 4 depicts the difference in the PL properties of the nanosized and bulk $Y_2Sn_2O_7$ and Gd_2O_3.

Figure 5 shows the manner in which concentration quenching can be altered in nanostructured materials compared with that in their bulk counterparts. In a bulk material, due to the close proximity of the energy levels of dopants, the excitation energy can propagate over large distances before being quenched by the nonradiative center. In NPs, the energy level of the dopant ions significantly differs due to structural disordering. Further, the propagation of excitation energy is blocked at a short distance.

In addition, the nature of the scintillating materials is important, i.e., whether it is a single crystal, powder, pellet, polymer, gel, or ceramic. Figure 6 shows the RL spectra of LuAG:Ce:Tb ceramic and single crystal [111]. Single-crystal LuAG:Ce:Tb demonstrated better performance in terms of spectral purity and intensity when compared with the ceramic. Specifically, the LY of the LuAG:Pr single

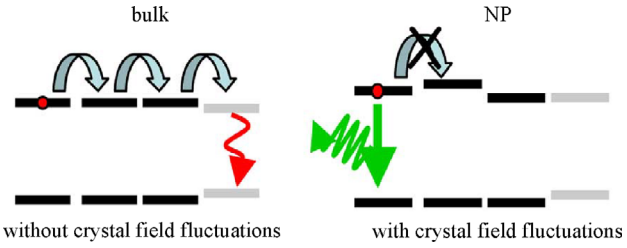

Fig. 5 De-excitation process of nanosized and bulk crystals under the influence of crystal field fluctuation [101]. Copyright 2010. Reproduced with permission from IEEE

crystal was 15600 Nph/MeV, whereas that of the LuAG:Pr ceramic was 7200 Nph/MeV. Nph is the number of generated photons in a scintillation flash. The LY of the LuAG:Ce single crystal was determined to be 25500 Nph/MeV, which is considerably higher than that of the LuAG:Ce ceramic [112]. On the other hand, the LY of LuAG:Ce, Tb ceramic was low (only ~4000 Nph/MeV). Such a reduction in LY after co-doping can be attributed to the inefficient energy transfer from the Ce^{3+} site to the Tb^{3+} site [113]. Moreover, the better performance of single crystals over ceramics can be attributed to the undesirable scattering of emitted photons from the surface defects, grain boundaries, and voids in the ceramic materials.

Cost-effective nanoceramic materials are preferred in case of advanced technological applications, such as PET, because of the high cost required for producing single-crystal scintillators. The less time required to prepare nanoceramics when compared with that required to prepare single crystals makes them more attractive for usage in nanoscintillator applications. Further, they fulfill other requirements such as high density, fast response time, good

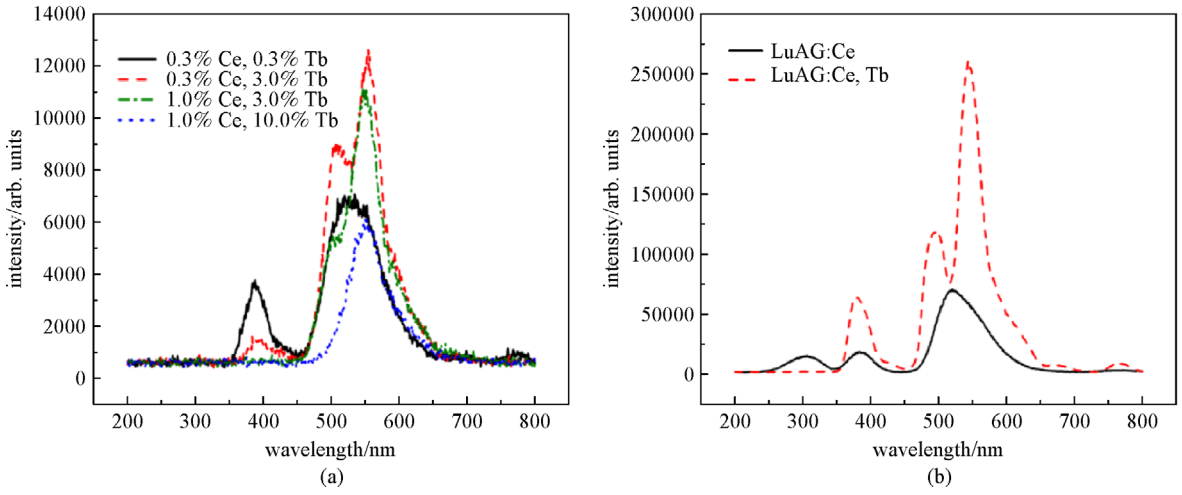

Fig. 6 RL spectra of (a) the LuAG:Ce:Tb powder and (b) single crystals [111]

energy resolution, and low production cost. The only disadvantage of ceramic materials is their low optical transparency compared with that of the BSCs; therefore, their light output is relatively low. This causes light scattering at the grain boundaries arising from the mismatch of refractive index among the grains misaligned in birefringent materials. This results in long escape paths for light and considerable amount of self-absorption of light in opaque ceramic materials. Moreover, if any impurities are present at the grain boundaries, the nonradiative recombination of excitons occurs, reducing the scintillation efficiency. There are two design approaches for obtaining good nanoceramic scintillators: the usage of (i) nanocrystalline birefringent materials and (ii) optically isotropic cubic materials. Nanocrystalline materials are transparent because the length scale over which the refractive index variations occur is considerably less than the wavelength of light. They appear to be a homogeneous transparent effective medium [114].

2.2 Surface effect

The surface states considerably influence the optical properties of NPs due to their high S/V ratio. The surface defects act as luminescence-quenching centers by providing a nonradiative pathway. The high mobility of excitons increases their probability to reach the surface of the NPs. In case of activated compounds, the fraction of activator ions near the surface in nanomaterials is high. All these factors lead to luminescence quenching aided by the surface defects in nanoscintillators, which should be considered to improve the scintillation efficiency.

To eliminate surface defects, there are several strategies such as coatings, the core–shell approach, and polishing. The core–shell approach is the most predominant technique used in nanotechnology to eliminate surface defects. The shell can be crystalline [115] or amorphous [116,117]. Surface coating is another technique that can be used to control the surface-defect-related quenching in NPs. Moreover, it improves the thermal and moisture resistance properties of the NPs [118–122]. For example, coating nanoscintillator particles with a thin mesoporous layer of silica significantly improves the PL emission intensity when compared with that of the bare scintillating NPs [123]. The hydroxyl ion on the surface of NPs can cause luminescence quenching; therefore, nanoscintillator particles in such a way that the OH group should be completely removed from their surface.

When materials exhibit a high intrinsic quantum yield (QY), reducing the size of nanoscintillators will not improve the QY. To preserve the luminescent efficiency of nanoscintillators by improving their surface states, various nanoengineering approaches, such as surface passivation, shape optimization, and surface charge optimization, have been explored. In case of a specific active site, symmetry is observed near the surface of the NPs and the luminescence intensity is correlated with the number of surface atoms [124]. The surface of NPs is a key factor that should be considered to perform fine spectroscopy and comparison of the bulk particles and NPs [125]. Figure 7 shows the manner in which the core–shell approach improved the scintillation/emission efficiency of nanoscintillators, such as $La_2Zr_2O_7:Eu^{3+}$ NPs [126], $Gd_2O_3:Eu^{3+}$ NPs [127], and $BaF_2:Ce^{3+}$ NPs [5,127,128].

Due to the luminescence quenching caused by the surface defects (dangling bonds and absorbed species) or disorders in the lattice surrounding the activator ions, PL efficiency was lower in NPs when compared with that in larger sized or bulk materials [118,129–133]. There are various methods, such as surface modification and the core–shell approach, to improve the optical properties of the NPs [134]. Jacobsohn et al. synthesized RE-doped fluoride nanoscintillators by exploiting the core–shell approach [134]. They observed a substantial increase in

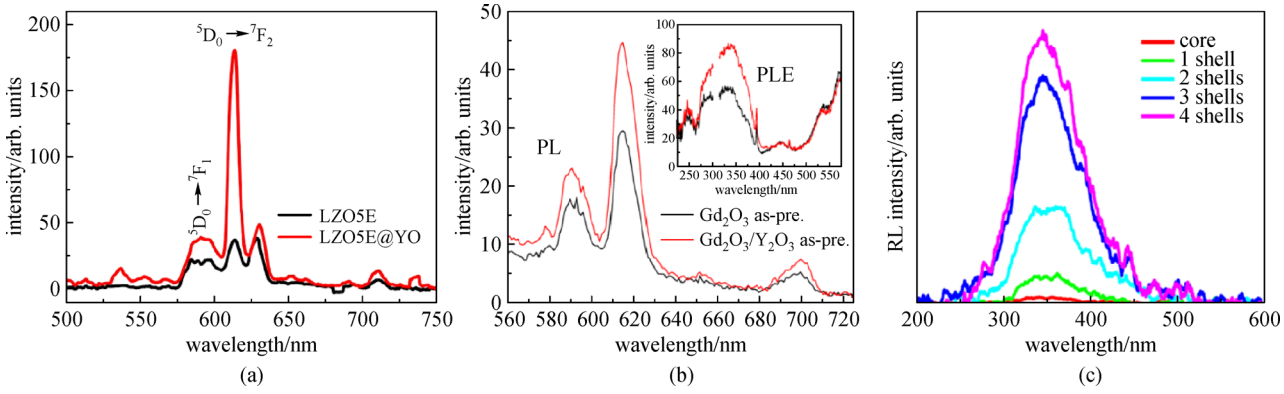

Fig. 7 RL spectra of (a) $La_2Zr_2O_7:Eu^{3+}$ NPs [126] (Copyright 2011. Reproduced with permission from Elsevier), (b) $Gd_2O_3:Eu^{3+}$ [127] (Copyright 2013. Reproduced with permission from the Department of Materials Science and Engineering, University of Florida, Gainesville, Florida) and (c) $BaF_2:Ce^{3+}$ NPs [127] (Copyright 2013. Reproduced with permission from the Department of Materials Science and Engineering, University of Florida, Gainesville, Florida)

the scintillation output, which was attributed to the increase in the volume of the NPs, causing radiative emission. Large NPs can accommodate large irradiation cascade fractions. When their dimensions approach the mean recombination length of the e^-–h^+ pairs, the radiative recombination probability increases and the luminescence centers in the core remain unaffected by the surface defects of the NPs [128,134]. The presence of various layered structures in NPs influences the scintillation parameters, light output, scintillation kinetics, and radiation stability. The improvements in important scintillation parameters, such as the LY, scintillation kinetics, and radiation hardness, are the main reasons for their improved and better performance [135]. Some of the examples where these parameters were optimized to achieve better scintillator efficiency are $Gd_2O_2S:Eu^{3+}$ NPs [123], $Gd_2O_3:Eu^{3+}$ NPs [136], fluoride nanoscintillators [5,95,128,134], and HfO_2 NPs [99,137]. The RL spectra of several nanoscintillators of doped metal oxides, doped metal fluorides, and undoped metal oxides are shown in Fig. 8.

2.3 Quantum confinement

When the size of NPs is smaller than the exciton Bohr radius, the electron is confined in a potential box and the quantization of the momentum distribution of electrons occurs. This phenomenon is called quantum confinement and exists mostly in semiconducting nanocrystals. Classical mechanics is no longer valid, and quantum mechanics can be observed to become influential. Because of quantum confinement, researchers have found a manifold increase in the light emission efficiency of semiconductor nanostructures in comparison with their bulk crystals [138]. In semiconductor NPs, the light conversion efficiency increased mainly due to two reasons: (a) electron and phonon quantum confinement caused by the nanodomain of the emitters, which increases the probability of the radiative recombination of excitons and (b) the usage of nano-resonator arrangement to increase the density and spontaneous light emission probability of virtual photons [135]. The same analogy can be applied to nanoscintillators because the light emission processes in both the cases (semiconductor NPs and nanoscintillators) are similar. The only difference is obtained with respect to the energy pumping methods, i.e., the semiconductors are pumped by electrical or optical methods (depending upon the type of luminescence), and the ionizing radiation stimulates scintillation. Currently, many researchers have reported the exploration of nanoscintillators for multifunctional applications [70,82,93–94,104–107].

The synthesis of YAG:Eu in the nanodomain significantly increases the efficiency of scintillation compared to single crystals [139]. They also observed that the Lu- and Gd-doped YAG nanoscintillators exhibit improved scintillation efficiency when compared with that exhibited by their bulk counterparts or single crystals [139]. The size of both the NPs is 70–100 nm, which is much larger than the quantum confinement size scale (< 10 nm). However, when the size of the NPs is much greater than that of the Bohr exciton, a weak confinement zone is reported [140]. In such cases, NPs display the Rashba effect through which electron excitation polarizes the NPs where they are confined [141]. The Rashba effect explained the momentum-dependent splitting of spin bands in a two-dimensionally condensed phase such as heterostructure and surface states, similar to the Dirac Hamiltonian splitting of particles and antiparticles.

Recent advancements in nanotechnology have opened new avenues to control material synthesis at the molecular level by optimizing various parameters [115,142–145]. The size, shape, temperature, surface charge, and composition of a wide variety of nanomaterials as well as the synthesis parameters, such as pH and processing time, can be tuned to yield novel properties because of the combined effect of S/V ratio and quantum confinement. In case of

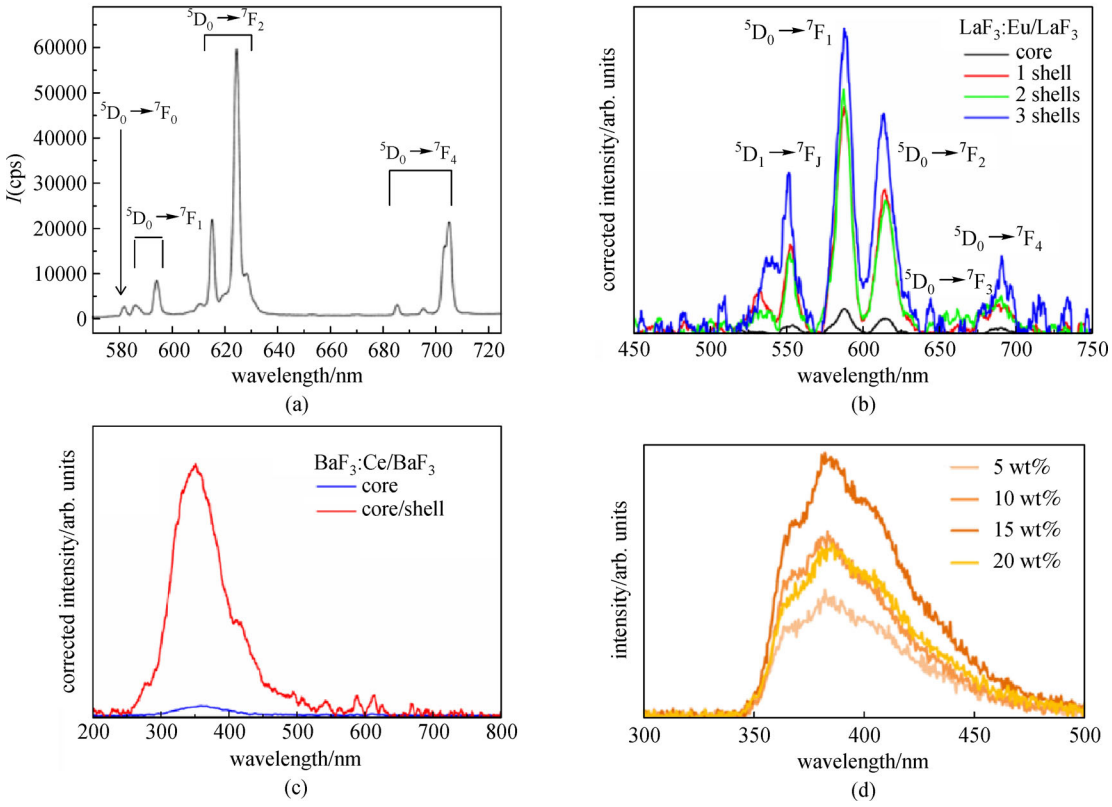

Fig. 8 RL spectra of (a) $Gd_2O_2S:Eu^{3+}$ NPs [123] (Copyright 2011. Reproduced with permission from the Royal Society of Chemistry), (b) $LaF_3:Eu^{3+}$ NPs [128] (Copyright 2010. Reproduced with permission from IEEE), (c) BaF_3:Ce NPs [128] (Copyright 2010. Reproduced with permission from IEEE), and (d) HfO_2 NPs [137] (Copyright 2017. Reproduced with permission from the Japan Society of Applied Physics)

semiconductors, when the particle size is less than 10 nm, quantum confinement effect dominates, where their bandgap can be widened by reducing their particle size, which can lead to visible emission and its exploration as scintillators. Létant et al. recently demonstrated the ability of the CdSe/ZnS core–shell QDs to work as a scintillator and conversion of the α and γ radiations into visible photons (Figs. 9(a) and 9(b)) [146]. They observed that the performance of the CdSe/ZnS core–shell QDs is two times better than that of the NaI(Tl) detector in terms of the scintillation efficiency. Shibuya et al. observed a decay component of 390 ps even at room temperature (Fig. 9(c)) [147]. This response is much faster than that observed in case of conventional Ce^{3+}-doped scintillators, which can be attributed to the quantum confinement effect that increases the electron and hole wave-function overlapping region in the low-dimensional system. Liu et al. demonstrated increased light output obtained from a scintillator film made of CdSe/ZnS QDs in the normal direction using photonic crystal structures [148]. They achieved a twofold enhancement of emission light from the wavelength-integrated emission spectra by controlling the photonic crystal structure under the excitation of UV light and X-rays, which is beneficial in case of radiation detection applications.

2.4 Dielectric confinement

The probability of influencing the effective electron–electron interaction strength between two charged particles in a dielectric material is known as dielectric confinement. This is realized by surrounding (embedding or confining) a dielectric medium with a material of dielectric constant ε. The strength of the effective electron–electron interaction in a dielectric material having a dielectric constant ε is proportional to $1/\varepsilon$ [149].

According to Fermi's golden rule, the spontaneous rate of emission of an emitting ion is directly proportional to the local electric field [101]. In any material, this effect is related to its refractive index and the radiative lifetime of the fluorophore, which depends on the refractive index of HL. Moreover, the lifetime of NPs strongly depends on its local surroundings because the luminescent NP sizes are smaller than the spatial extension of the electric field. This phenomenon has been observed in many cases such as QDs [150], normal/reverse micelles [151], and activator-doped insulators [152,153]. Scintillation properties can also be optimized by only changing the HL, such as fluorides and oxides, because they have different refractive indices, local fields, and phonon energy. Figure 10 shows the manner in which the bandgap of the ZnS:CdTe

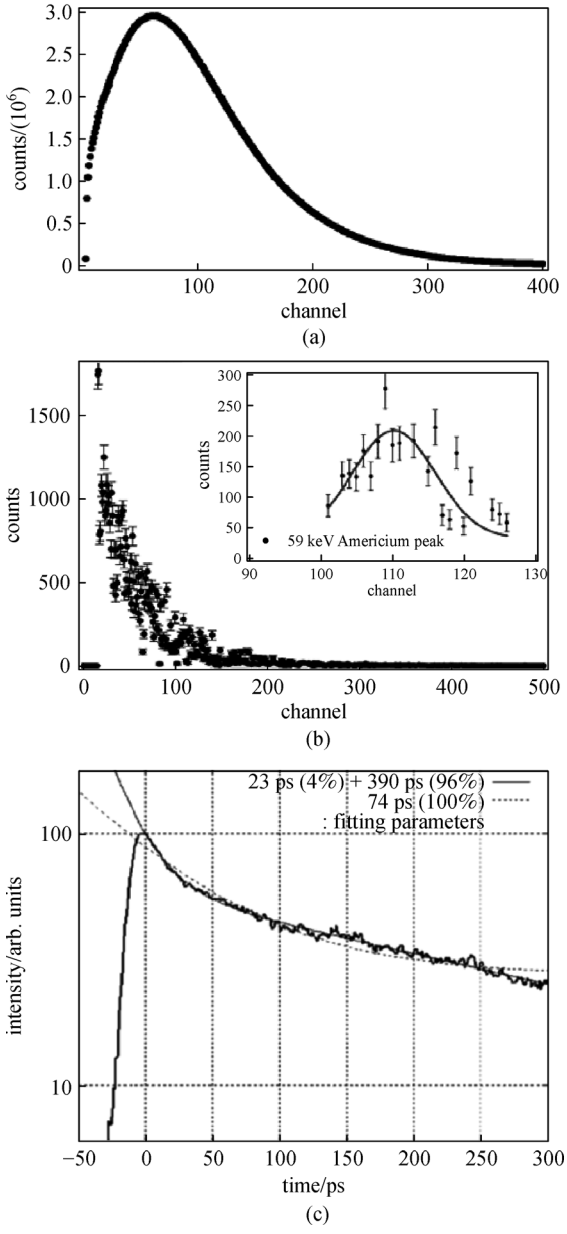

Fig. 9 Scintillation output of the quantum dot nanoporous glass composites under (a) α and (b) γ irradiation. Both the pulse height spectra were corrected from the background radiation. A Gaussian fit of the 59-keV line of americium-241 shown in the inset indicates an experimental energy resolution $\Delta E/E$ of 15% at this energy [146] (Copyright 2006. Reproduced with permission from the American Chemical Society). (c) Scintillation temporal behavior of $(n\text{-}C_6H_{13}NH_3)_2PbI_4$ measured with the streak camera and fitted with the sum of two or one exponential decays [147] (Copyright 2014. Reproduced with permission from the Japan Society of Applied Physics)

nanocrystals can be tuned by incorporating a dielectric medium between them. Bandgap has significant influence on their scintillation properties [154].

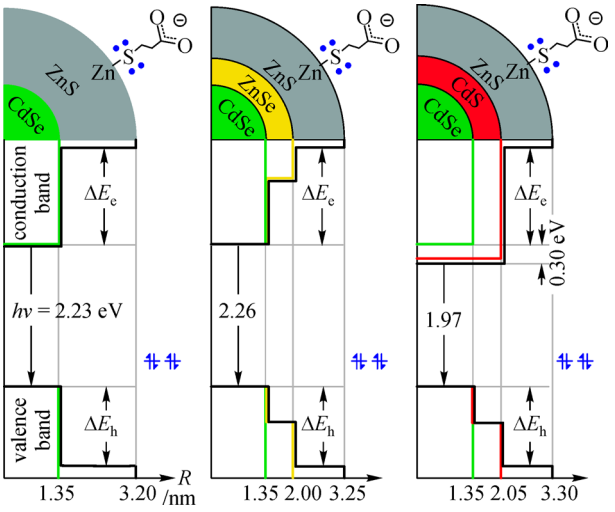

Fig. 10 Band energy diagrams of the CdSe/ZnS, CdSe/ZnSe/ZnS, and CdSe/CdS/ZnS nanocrystals [154]. Copyright 2010. Reproduced with permission from PCCP Owner Societies

3 Various compositions of nanoscintillators

3.1 Oxide-based nanoscintillators

Among bulk oxide-based scintillators, several aluminum-oxide-based hosts have attracted a lot of interest because of their excellent performance [155–158]. Particularly, crystals, such as YAG ($Y_3Al_5O_{12}$) and lutetium aluminum garnet ($Lu_3Al_5O_{12}$, LuAG), have been extensively studied because of their easy growth. Other aluminum oxides, such as gadolinium gallium aluminum garnet ($Gd_3Ga_3Al_2O_{12}$:Ce, GGAG), exhibit a high LY of 60000 ph/MeV. This can be attributed to the considerable decrease in defect concentration below the bottom of the CB, preventing ionization-induced quenching of the excited 5d level of the Ce^{3+} activator ions.

The lifetime of the Ce^{3+}-doped oxide scintillators is approximately 40–100 ns. Scintillators with an even shorter lifetime are required to shorten the time gate and utilize the time of flight. To achieve shorter decay time, we must explore the relation between the transition probability and emission wavelength. A high luminescence efficiency of approximately 300 nm is normally compatible to ensure fast decay time and detection in case of conventional PMT. To meet such demands, $5d \rightarrow 4f$ luminescence of Pr^{3+} was selected. The Pr^{3+} ion exhibits $5d \rightarrow 4f$ luminescence, similar to that exhibited by Ce^{3+} in some HLs. However, the energy gap between the $5d \rightarrow 4f$ excited state and the 4f ground state of Pr^{3+} is larger than that in case of Ce^{3+}. This is responsible for the expectation of shorter decay time. In addition, there are many restrictions on host crystals for achieving Pr^{3+} luminescence when compared with the $5d \rightarrow 4f$ luminescence of Ce^{3}. Wide-bandgap hosts and

high crystal field are required. Many 4f levels interfere with the fast 5d → 4f luminescence. For obtaining efficient 5d → 4f luminescence from Pr^{3+}, $Lu_3Al_5O_{12}$ (LuAG) was found to be the best host. Under UV excitation, LuAG:Pr^{3+} had a decay time of less than 20 ns and an LY more than three times higher than that of the conventional BGO.

To date, few studies have investigated the RL of NPs. The pyrochlore-based compound of lanthanum hafnate ($La_2Hf_2O_7$) has been extensively explored as a scintillator host because of its high density and large effective atomic number. Our group has developed Pr^{3+}- and Eu^{3+}-doped $La_2Hf_2O_7$ nanoscintillators with their RL spectra shown in Figs. 11(a) and 11(b), respectively [33,40,160]. Moreover, the RL properties of the microcrystalline $La_2Hf_2O_7$:Ce powder were investigated (Fig. 11(c)) [159]. Interestingly, the bulk $La_2Hf_2O_7$ powder shows green RL (Fig. 12(c)), unlike nanocrystalline $La_2Hf_2O_7$.

3.2 Fluoride-based nanoscintillators

As discussed earlier, the main scintillation processes are conversion, transfer, and luminescence. The appropriate selection of the host matrix is essential to achieve high scintillation efficiency because the distance between the dopant ions in doped phosphors, the relative spatial distribution of the dopants, the local coordination number, and the environment of the dopants are determined by HL. The main features of an ideal HL include transparency with respect to the spectral range of interest, high optical damage threshold, low phonon energy, and thermal, chemical, and mechanical stability. Even though the appropriate selection of hosts and dopant ions dictates the efficiency of the conversion and luminescence processes in scintillators, a unique aspect of the scintillation process in NPs is related to the migration of carriers via nanoscintillators. Fluoride HLs have low phonon energy compared to that of oxide hosts because fluorine is heavier than oxygen, which allows better radiative recombination and scintillation efficiency due to the less vibration observed in fluorides [161]. The net scintillation efficiency is mainly determined by the radiative recombination at the luminescence active center versus the nonradiative recombination at the luminescence-quenching centers, particularly on the surface of NPs. The *e*–*h* pair

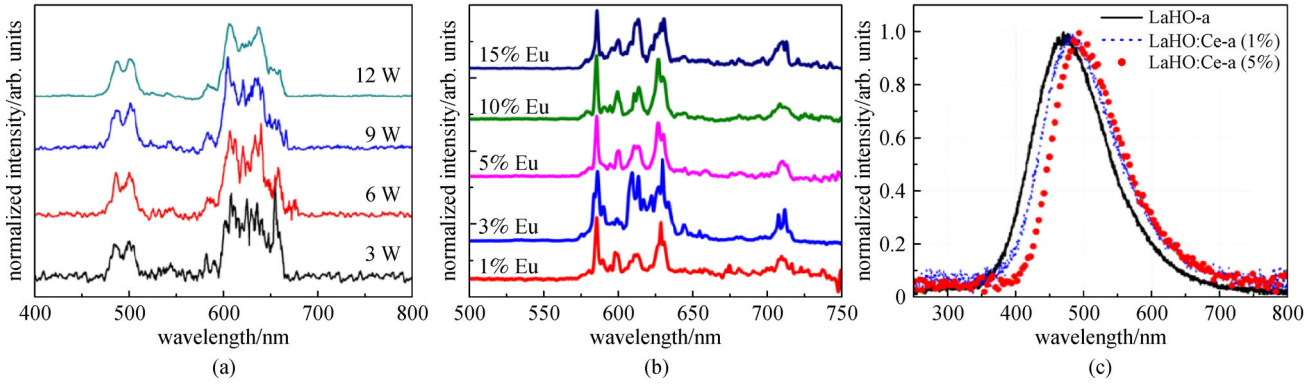

Fig. 11 RL spectra of the (a) $La_2Hf_2O_7:Pr^{3+}$ NPs [36] (Copyright 2018. Reproduced with permission from Royal Society of Chemistry), (b) $La_2Hf_2O_7:Eu^{3+}$ NPs [40] (Copyright 2017. Reproduced with permission from Elsevier), and (c) $La_2Hf_2O_7:Ce^{3+}$ bulk microcrystalline powder [159] (Copyright 2012. Reproduced with permission from Elsevier)

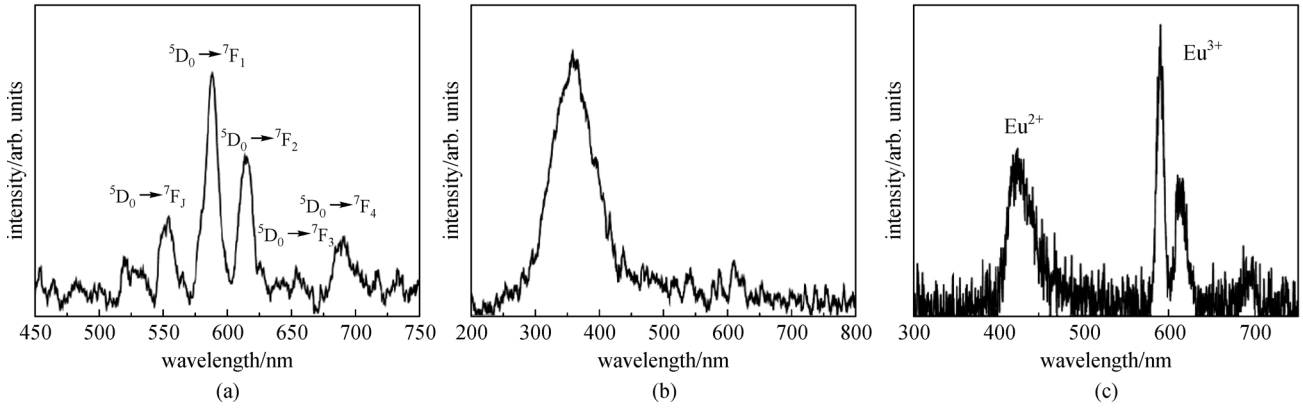

Fig. 12 RL spectra of the (a) LaF_3:Eu, (b) BaF_2:Ce, and (c) CaF_2:Eu nanoscintillators [5]. Copyright 2011. Reproduced with permission from Hindawi

diffusion length of alkali halides is approximately 100 nm [162], whereas those of oxides and oxysulphides decrease to 10 nm [163,164]. This suggests better efficacy of fluorides when compared with oxides and other hosts. When the size of NPs is considerably smaller than the diffusion length of the *e*–*h* pairs, the scintillation process is efficient, which is concomitant to a relatively high probability of nonradiative recombination on the surface of NPs. Such approach should be taken care of when designing NPs for radiation detection. The scintillation response of CaF_2:Eu NPs under ^{241}Am irradiation has been discussed previously [5].

Figure 12 shows the RL spectra of different fluoride NPs [5]. When RE ions, such as cerium and europium, are introduced into fluoride NPs as hosts with low phonon energy, efficient scintillation is expected. The low phonon energy of fluoride nanocrystals can minimize the non-radiative path and enormously enhance the emission efficiency of the lanthanide ions [161].

3.3 Organic–inorganic nanocomposites (OINC)

A new category of smart materials, which are composites of inorganic and organic compounds termed as organic–inorganic nanocomposites (OINCs), have become popular recently. These hybrid compounds have the combined benefits of inorganic and organic moieties; therefore, the designed smart materials have diverse and interesting properties. Inorganic constituents provide higher light emission output and tunable bandgap or luminescence, whereas organic constituents provide high optical transparency, biofriendliness, high mechanical and radiation stability, high laser damage threshold, low cost, high level of flexibility, large size, and ease of synthesis [165]. The combined advantages of ISs and OSs make them excellent scintillation candidates. OINCs are normally inorganic constituents dispersed in matrices of organic polymers; for example, barium and strontium fluorides are dispersed in the polystyrene matrix [166,167].

However, it is often difficult to homogeneously disperse inorganic NPs into organic polymer matrices and maintain transparency. Considering their application as scintillators, OINCs have many advantages, particularly in the fields of imaging, radiography, tomography, and security [168,169]. In case of X-ray imaging, OINCs have shown exemplary potential and capability to replace the existing materials [170–172].

In radiography, the existing devices mostly employ CsI:Tl thin films or Gd_2O_2S single crystals as imaging screens [173]. However, it is difficult, time-consuming, and expensive to obtain large-area imaging screens using single-crystal scintillators. Thus, OINCs can be a feasible option [170]. In case of industrial radiography, OINCs have several advantageous properties, such as superior optical properties, flexibility, and high radiation stability. Moreover, they exhibit cost efficiency with respect to industrial applications. The thickness of OINCs is suitable for X-ray imaging. They should be sufficiently thick to stop X-rays and sufficiently thin to not adversely affect the spatial resolution of formed images.

RL spectroscopy was conducted with respect to various OINCs to evaluate their scintillation properties (Figs. 13(a)–13(c)). The RL spectra of PMMA:$Gd_3Ga_3Al_2O_{12}$:Ce (GGAG:Ce) film displayed a broad emission peak at approximately 550 nm (Fig. 13(a)). It is attributed to LaPorte allowed f–d transition of trivalent Ce^{3+} ion. Figure 13(b) displays the RL emission spectra of another type of OINC films, where BaF_2 NPs having different sizes were dispersed in polystyrene (20–100 nm). As a function of the particle size, the RL intensity changed only slightly with respect to these samples. The RL intensity of the BaF_2 NPs upon X-ray irradiation decreased substantially when their size was less than 20 nm [174,175]. However, such dependence could not be

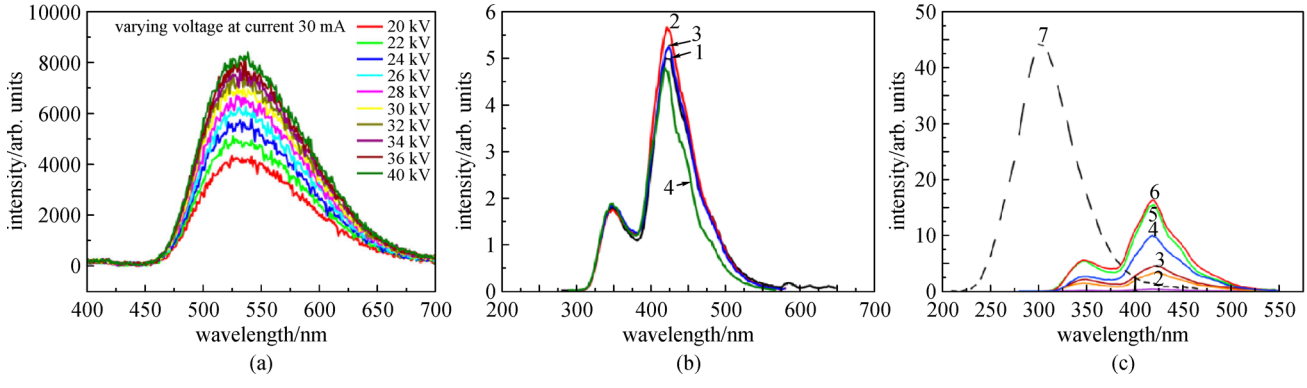

Fig. 13 RL spectra of (a) PMMA:$Gd_3Ga_3Al_2O_{12}$:Ce (GGAG:Ce) film under different X-ray tube voltages [165] (Copyright 2017. Reproduced with permission from the American Chemical Society), (b) BaF_2 NPs:polystyrene film having different NP sizes [166] (Copyright 2016. Reproduced with permission from Elsevier), and (c) SrF_2 NPs:polystyrene film having different NP sizes. Curve 7 represents the spectrum of the SrF_2 microcrystalline powder pellet having the same thickness as the film [167] (Copyright 2017. Reproduced with permission from Elsevier)

observed when they were dispersed in the polystyrene matrix. As shown in curve 1 of Fig. 13(c), the RL intensity of the bare polystyrene film without NPs is extremely low because of its low X-ray absorption coefficient (effective Z = ~6). On the other hand, when 40 wt% SrF_2 NPs is dispersed in the polystyrene matrix, the RL intensity of such OINCs significantly increases due to the substantial increase in effective Z from 6 to 38 (Fig. 13(c)). An order of magnitude enhancement is obtained with respect to the luminescent intensity of polystyrene by adding SrF_2 NPs.

3.4 Cluster compounds

Organic crystals are normally considered to be good scintillators in case of low-energy β-rays and neutrons because of their high neutron and electron scattering cross sections and low background from backscattering [176,177]. Anthracene is an efficient and well-studied organic crystal. However, organic crystals are not suitable for X-ray detection because of their low X-ray scattering cross section, particularly for X-rays having energy < 100 keV. On the other hand, metal–organic frameworks (MOFs), as a new class of organic compounds, have been demonstrated as good alternatives for OSs [31]. Because of high atomic numbers (Z_{eff}) and highly ordered structures, MOFs can provide a tunable platform to OSs and metal clusters [178]. For example, zinc–MOFs are excellent scintillating materials to detect the β-, n-, and γ-rays [179,180]. MOFs are more applicable than organic crystals as scintillators because of the large spatial separation of the scintillating molecules, which causes the high RL efficiency and radiation stability [181–183]. In organic crystals, excitation energy delocalizes and randomly moves throughout the crystals. The ionizing radiation induces the formation of defects within them. These defects slowly accumulate and efficiently quench the delocalized excited energy by providing nonradiative pathways. MOFs have high radiation stability due to their highly open and ordered structures that restrict the mobility of the excitation energy.

Hf and Zr have large X-ray absorption cross sections with high Z_{eff} values of 72 and 40, respectively. When they are linked with organic ligands, such as anthracene, scintillation/RL occurs via the ejection of the valence electrons of the Hf^{4+} and Zr^{4+} ions upon X-ray irradiation. For obtaining efficient X-ray luminescence from MOFs, efficient synergy should be achieved between metallic clusters and organic ligands. Figure 14(a) shows the scheme for the synthesis of Hf–MOF and Zr–MOF, and Fig. 14(b) displays the scheme in which Zn–anthracene MOFs exhibit efficient luminescence under X-ray excitation. Symbiosis can be observed between the heavy metal ions and organic linkers. Photoelectrons are ejected from the heavy Zr^{4+} and Hf^{4+} ions upon X-ray irradiation followed by light emission by the anthracene-based linkers. The photoelectrons generated from the heavy metal ions undergo non-elastic scattering in MOFs followed by photon energy transfer to the bridging ligands, which result in their migration to high-energy excited states. Subsequently, the photoelectrons relax and emit visible photons for detection. Because of these favorable properties, MOFs can serve as efficient X-ray antennas.

Hf–MOF and Zr–MOF display bright visible light upon X-ray excitation (Fig. 15(a)). Because the Z_{eff} of Hf is higher than that of Zr, the X-ray scintillation efficiency of Hf–MOF is better than that of Zr–MOF. In the 15–30-keV range, the average X-ray energy attenuation coefficient for Hf ranges from ~110 to 18 cm^2/g, whereas that for Zr ranges from ~23 to 16 cm^2/g [184]. Figure 15(b) shows the RL signals emitted from Hf–MOF and Zr–MOF having different metal concentrations and X-ray tube voltages.

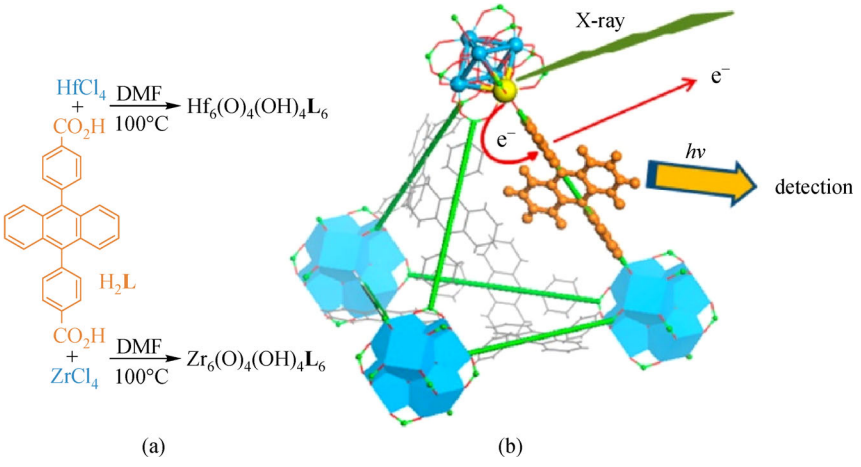

Fig. 14 (a) Synthesis of Hf–MOF and Zr–MOF and (b) X-ray-induced generation of fast photoelectrons from heavy Hf and Zr metals followed by the scintillation of the anthracene-based linkers in the visible spectrum [31]. Copyright 2014. Reproduced with permission from the American Chemical Society

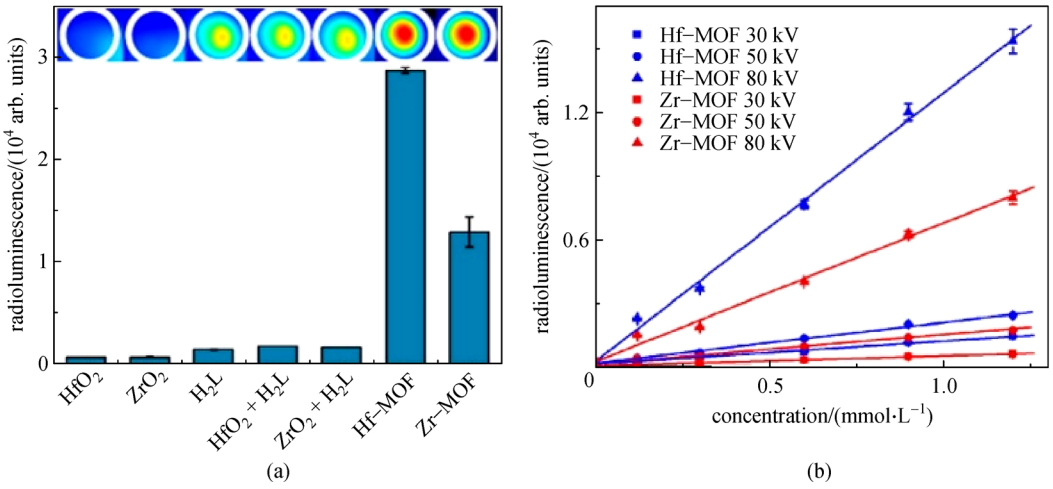

Fig. 15 (a) RL signals of the Hf–MOF, Zr–MOF, and control samples (from left to right): HfO_2 and ZrO_2 colloidal NPs, H_2L alone, HfO_2+ H_2L colloid, ZrO_2+ H_2L colloid, Hf–MOF, and Zr–MOF. The concentration of H_2L, Hf, or Zr in the samples is 1.2 mM. The X-ray dosages are 1 Gy/10 s with an effective X-ray energy of ~18.9 keV (40-kV tube voltage and 0.08-mA tube current) and a detection gain of 200. (b) RL signals of Hf–MOF and Zr–MOF with different concentrations and radiation tube voltages [31]. Copyright 2014. Reproduced with permission from the American Chemical Society

4 Physical forms of nanoscintillators

4.1 Nanoparticles (NPs)

As discussed, designing scintillating materials at the nanoscale has obvious advantages. Therefore, it becomes imperative to control the dispersion of dopant ions in the host matrix and the size, shape, and surface of the NCS grains. During the preparation of transparent ceramics that can replace single crystals, the most important advantage is that scintillators can be designed scintillatorsin the nanodomain. There are limitations with respect to the X-ray-excited optical luminescence owing to the NP size [5,185–188]. Some reports on the RL of fluoride, oxide, and phosphate NPs have denoted the effect of the scintillation efficiency as a function of NP size [174]. The surface area, particle size, and mean free path (λ) of the photoelectrons formed via X-ray absorption and the thermalization length (l) of electrons play decisive roles with respect to the determination of the efficiency of optical scintillation.

The luminescence intensity decreases significantly when λ and l are comparable with the NP size. This usually occurs when the photoelectrons or thermalized electrons are localized at large defect sites located on the surface of the NPs. For an X-ray photon of 40 keV, λ of the photoelectrons would be approximately 30–40 nm [189]. Within small NPs, electron–hole recombination does not occur at such a value of λ; instead, the excitation energy is exchanged among the neighboring NPs. This continues until the excitation energy becomes less than the work function of NPs due to electron–electron and electron–phonon scattering. The secondary electron and hole can be observed in different NPs. Radiative recombination is not allowed in such an exchange. With the decreasing NP size, the observation probability of a thermalized electron and hole in different particles increases, decreasing the luminescence intensity. The luminescence intensity threshold should reflect the parameters of the electron–hole separation distance in NPs; thus, the RL intensity is dependent on the NP size [190].

When incorporating NPs into a medium, such as polymers, fibers, films, and glass, the electrons leaving NPs could be visualized. Figures 16(a)–16(c) show the RL spectra of BaF_2, CaF_2, and $LuPO_4$:Ce, respectively. With X-ray excitation, the RL spectra of the BaF_2 NPs with different particle sizes showed a behavior typical of the bulk BaF_2 crystal (Fig. 16(a)) [174]. The emission spectra have two bands at 225 and 300 nm, which can be attributed to the recombination of electrons and holes (V_k center). The emission band at 300 nm can be attributed to the self-trapped excitons (STEs). During the recombination of electrons from the 2p F^- VB and the holes of the 5p Ba^{2+} core band, the emission maxima at 225 nm can be attributed to the core valence luminescence (CVL) [6]. The reduction in particle size decreases the luminescence intensity of STE and CVL (Fig. 16(a)). When the particle size becomes less than 80 nm, the STE intensity was observed to drastically decrease. However, the rates at which STE and CVL decrease are different. The various natures of luminescent mechanisms in case of STE and CVL cause the different dependences of the luminescent intensity of STE and CVL on the NP size [185].

When the emission band is located at 300 nm, the RL profile of the CaF_2 NPs is similar to that of the CaF_2 single crystal (Fig. 16(b)) [186]. When the size of the NPs is 20–30 nm, the RL intensity is low and almost independent of the NP size. An increase in RL intensity is observed when

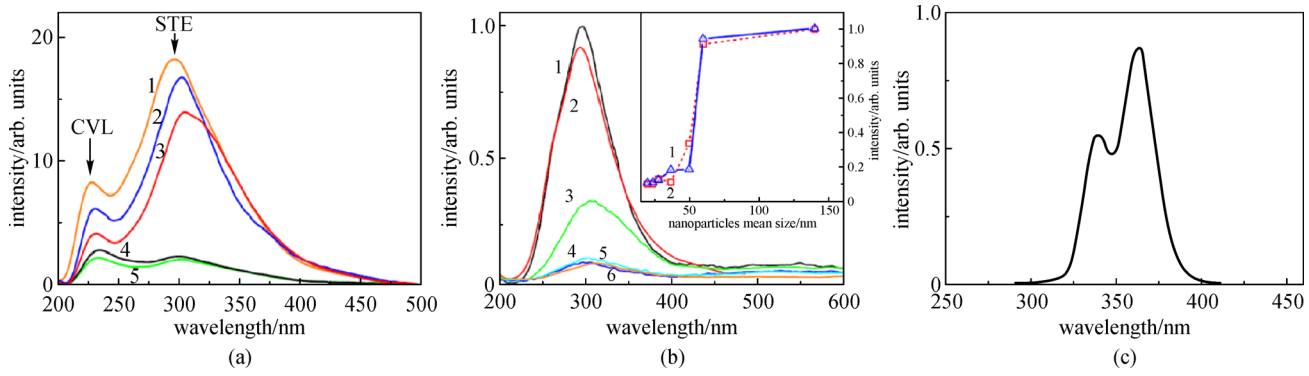

Fig. 16 (a) RL spectra of the BaF_2 NPs having different sizes [174] (Copyright 2014. Reproduced with permission from AIP), (b) RL spectra of the CaF_2 NPs having different sizes [186] (Copyright 2012. Reproduced with permission from AIP), and (c) RL spectra of the $LuPO_4$:Ce NPs [188] (Copyright 2014. Reproduced with permission from Elsevier)

the NP size exceeds 50 nm. λ of the photoelectrons becomes comparable or smaller than the sizes of the NPs, resulting in RL enhancement. When STE formation is observed within the NPs, the number of favorable situations for electron–hole recombination decreases.

The RL spectra of the $LuPO_4$:Ce NPs with mean sizes of approximately 35 nm and sub-12 nm under X-ray irradiation reveal the different structures of the cerium centers, as shown in Fig. 16(c) [186]. Upon excitation in the range of band-to-band transitions and under X-ray excitation, the luminescence efficiency of the sub-12-nm $LuPO_4$:Ce NPs substantially decreases.

4.2 Thin films

When compared with powder phosphors and conventional single crystals, thin-film scintillators have several unique advantages, such as exhibiting full transparency, high contrast, high spatial resolution, and low afterglow properties. RL microscopy (RLM) is one of the highly demanding and sophisticated techniques to achieve image radionuclide uptake at the single-cell level. When thick scintillators are used for RLM, light is emitted in all directions along the track. It becomes very difficult to localize the origin of the particles [191]. In comparison, when thin-film scintillators are used, light only emanates from the active volume of the scintillators, located in close proximity to the cells. Therefore, thin-film scintillators considerably enhance the localization of the emitting molecules. As shown in Fig. 17(a), the thin-film Lu_2O_3:Eu scintillator produces a truncated ionization track as compared to the longer ionization track produced by the thicker $CdWO_4$ scintillator [191]. The unique scintillation properties of the Lu_2O_3:Eu thin-film scintillator allow the capture of single positron decays. Despite being very thin, its sensitivity is four times better than that of a relatively thick $CdWO_4$ scintillator (Fig. 17(b)).

4.3 Nanoceramics

Tl-activated CsI and self-activated $CdWO_4$ are being used as single-crystal scintillators in detectors for commercial CT scanners. CsI:Tl exhibits high afterglow (0.3%) and radiation damage/hysteresis (13.5%) [65]. The

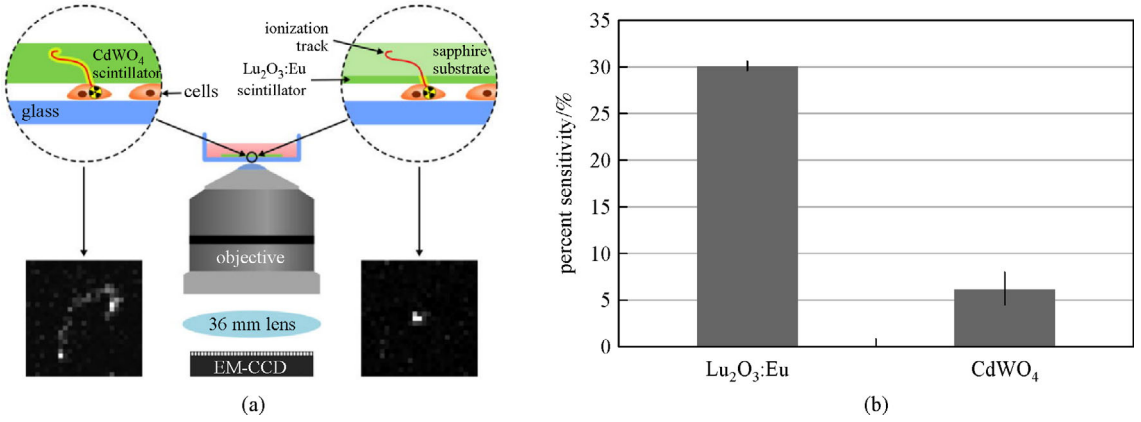

Fig. 17 (a) Schematic of a typical RLM setup using a 500-μm $CdWO_4$ scintillator (left) and a 10-μm Lu_2O_3:Eu scintillator (right). (b) Comparison of the sensitivities of the Lu_2O_3:Eu and $CdWO_4$ scintillators [191]. Copyright 2015. Reproduced with permission from John Wiley and Sons

image quality deteriorates because of these undesirable properties. Poor quality results in low light output (30% of CsI:Tl), decreasing the signal-to-noise (S/N) ratio. Because monoclinic $CdWO_4$ crystal has poor cleavage properties, it is difficult to design an actual device with desirable surface properties for scintillator applications. A high radiation damage of −2.9% can create image artifacts of $CdWO_4$. It is difficult to obtain uniform optical quality and activator concentration by growing large $CdWO_4$ single crystals.

The traditional ceramics comprising single or multiple crystalline and amorphous phases are normally translucent or opaque. Understanding the sintering process at the nanoscale has resulted in nanoceramics becoming available in various dimensions for several applications [192,193]. Meanwhile, highly dense monoliths of cubic micro/nanocrystals have resulted in advanced optically transparent ceramics (OTCs) with high transparency [194]. To fabricate OTCs, highly pure ceramic nanopowder is consolidated into a "green body" by pressing or casting. The "green body" is subsequently sintered and hot pressed to make them nonporous with near-full density. Single-crystal OTCs exhibit superior scintillation along with the ruggedness and processability of glass. Compared to single-crystal scintillators, ceramics offer the following advantages:

1) Increased flexibility with respect to scintillator composition because the precursor powder can be tailored to achieve specific need-based properties.

2) Lower processing temperature because it avoids a melt that is typically required for crystal growth and can potentially reduce the costs while increasing the yield.

3) Faster processing cycles, with the cycles being completed in hours instead of days.

4) Near-net shape fabrication, which reduces the machining costs and provides an ability to obtain complex shapes if required.

Lutetium oxide (Lu_2O_3) is a refractory oxide with a high density of 9.42 g/cm^3, an effective atomic number of 69, and a high melting point of 2490°C. These factors make its single-crystal synthesis considerably difficult and expensive; further, it requires a high stopping power with respect to γ- and X-ray radiation. The methods that can be used to fabricate the Lu_2O_3 OTCs in a highly pure and dense form of Lu_2O_3:5%Eu^{3+} with low optical scattering include flame spray pyrolysis, vacuum sintering, and hot isostatic pressing. As shown in Fig. 18, the LYs of the scintillating glass (Tb^{3+} activated silicate glass) and the Lu_2O_3:5%Eu^{3+} ceramic scintillator are 20000 and 75000 photons/MeV, respectively. Lu_2O_3:5%Eu^{3+} offers a potential improvement in throughput, almost ten times greater than that obtained using standard glass for performing high-energy scanning radiography.

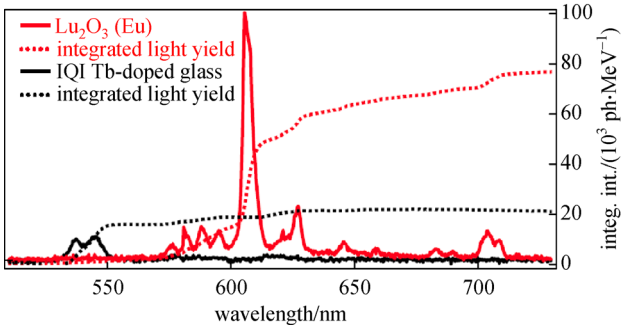

Fig. 18 Beta RL spectra of transparent 5% Eu-doped Lu_2O_3 ceramic compared with the Tb-doped glass scintillator along with their integral light yields [194]

4.4 Glass

Cerium-doped borosilicate glass was initially developed in the late 1950s as the first glass scintillator. Thereafter, glass scintillators have steadily advanced in terms of their efficiency, output, and performance. Their easy fabrication compared to other systems is one of the most important advantages that have facilitated the development of glass scintillators. Further, glass scintillators can be an integral part of PMT and tailored into any shape, size, and thickness. However, glass suffers from lack of long-range ordering, which does not allow energy transfer over a long distance when compared with crystals. This drawback leads to poor performance, low scintillation efficiency, and the lack of development of glass scintillators. Figure 19 shows the typical RL spectra of the phosphate and lead phosphate glass [195].

Controlled nucleation and crystallization of glass are required to produce glass ceramic (GC)-engineered materials. For GC fabrication, the melt quench technique is employed, and the sol–gel method is only occasionally used [196]. There are two heating steps that are used to control crystallization with respect to the amorphous glass, i.e., nucleation and crystal growth. Uniform dispersion of crystals throughout the glass matrix proceeds via this two-step heating process. By tuning the annealing temperature and composition of glass formers, several optical and mechanical properties can be achieved using GCs.

GCs are widely used for achieving controllable properties with the combined advantage of glass and sintered ceramics, which are suitable for γ-ray detection. The crystallites act as luminescent centers, and the glass matrix of GCs provides protection to scintillators from the outer environment, allowing encapsulation-free usage of the hygroscopic scintillating compounds. GCs do not cleave; therefore, they can be easily cut and polished, offering another advantage in addition to their mechanical stability, easy fabrication, and scalability. The production route of GCs allows for more compositional flexibility and can be highly useful for the production of compounds that do not melt congruently compared to the single-crystal growth methods. The cost of producing GCs is considerably less than that of the single-crystal growth methods used for

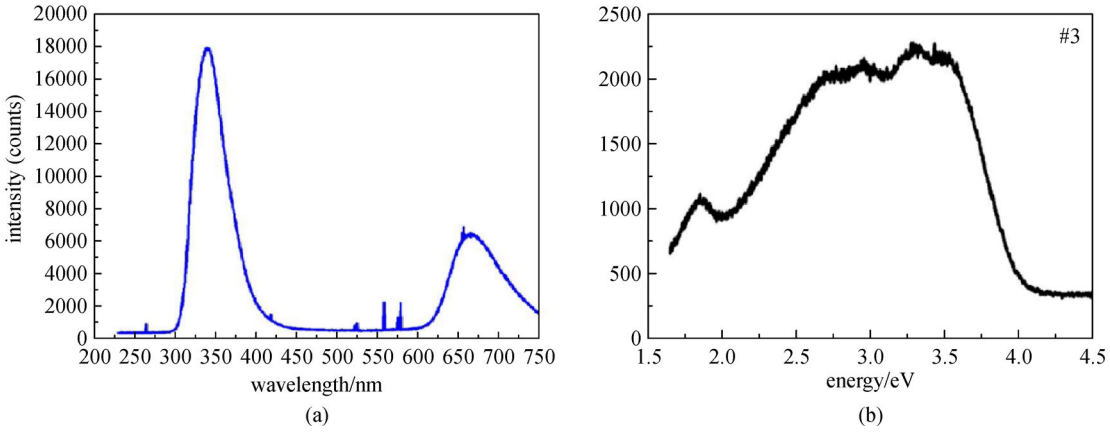

Fig. 19 RL spectra of (a) phosphate glass and (b) lead phosphate glass [195]

obtaining halide scintillators or the hot-pressing method used for obtaining polycrystalline ceramics.

The polymer-encapsulated nanocrystal scintillators are less efficient compared to the glass-matrix nanostructured materials in case of γ-ray detection because the latter has higher γ-ray attenuation [197]. The agglomeration in polymer-loaded NPs can be critical when compared with that in GCs because scintillating crystallites are formed *in situ* in GCs. Due to its high light output, GCs are preferred over bare glass for scintillator applications. The density of defect sites is large in the glass matrix for charge carriers. These defect sites can be non-bridging oxygen and impurities. They provide additional pathways for non-radiative recombination (phonon emission) and reduce light output. Therefore, bare glass scintillators exhibit low excitation energy transfer efficiency from the inorganic host to the luminescence active centers [198,199]. However, the crystalline phases in GCs have a considerably ordered nature. The crystalline phase offers efficient energy transfer from the host to the luminescent center. Therefore, the radiative recombination efficiency of GCs is relatively higher than bare glass [200]. Figure 20 gives the RL spectra of the Tb^{3+}-doped $Na_5Gd_9F_{32}$ GCs [201]. All the samples showed a dominant green emission of Tb^{3+} at 543 nm due to the $^5D_4 \rightarrow {}^7F_5$ transition. Hence, the as-synthesized GC samples can serve as scintillators for X-ray detection by converting X-ray radiation into green light. Other weak emission peaks of Tb^{3+} are visibly located at 383 nm ($^5D_3 \rightarrow {}^7F_6$), 415 nm ($^5D_3 \rightarrow {}^7F_5$), 437 nm ($^5D_3 \rightarrow {}^7F_4$), 458 nm ($^5D_3 \rightarrow {}^7F_3$), 489 nm ($^5D_4 \rightarrow {}^7F_6$), 588 nm ($^5D_4 \rightarrow {}^7F_4$), and 621 nm ($^5D_4 \rightarrow {}^7F_3$). The X-ray-excited optical luminescence had the same quenching concentration (4.0 mol%) as that of the PL spectra.

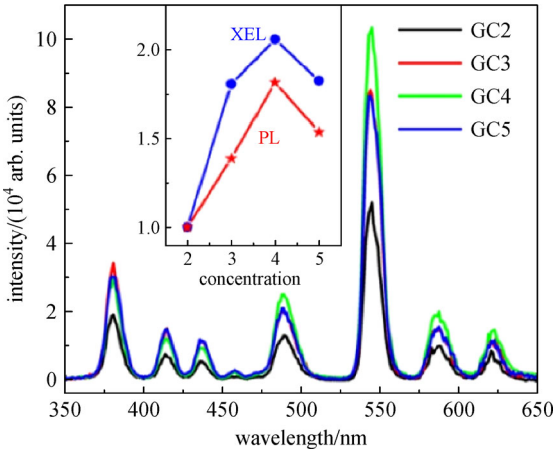

Fig. 20 RL spectra of the Tb^{3+}-doped $Na_5Gd_9F_{32}$ GC scintillators. The inset shows the dependence of the PL and XEL intensities on the Tb^{3+} concentration [201]. Copyright 2018. Reproduced with permission from the Optical Society of America

5 Applications of nanoscintillators

5.1 Ionizing radiation detection

By designing nanomaterials (nanoscintillators and nano-sized semiconductors) to detect ionizing radiation, the phonon-assisted losses are reduced, which are quite significant in case of single-crystal materials [202]. Therefore, a considerable amount of incident information can be converted into information carriers (charge and light) for signal formation. Many studies have addressed the usage of NCSs for radiation detection [99,202–205].

In an electromagnetic spectrum, the energy of an X-ray is very high compared to that of the UV light. The typical energy range for a UV/Vis/IR photon is between 1 and 5 eV, which matches with the bandgaps of the semiconductors, insulators, and doped alkali halides. Further, the energies of X-rays and γ-rays are between 0.1 and 200 keV; therefore, their spectroscopies involve inner electron and nuclear transitions. The γ-ray-based luminescence involves interactions between the photons and inner electrons of the scintillating atoms, including the photoelectric effect, Compton scattering, and pair productions. Because of the energy difference, the emission spectra

under excitation of UV light, γ-rays, and X-rays are different due to the fact that the mechanisms involved in these processes are different. For example, under X-ray excitation, the electron-hole pairs are generated from the Eu^{3+}-doped NPs, where the Eu^{3+} 4f–4f bands and hosts are excited. In this situation, the generated electrons migrate to the Eu^{3+} centers, whereas only the Eu^{3+} 4f–4f bands (but not the host) are excited under UV excitation.

The main phenomenon underlying the radiation detection and measurements depends on the name of radiation itself. Detectors sense the nonequilibrium ionized states induced in the interaction medium, i.e., the interactions of ionizing radiations, such as X-rays, β particles, or γ-rays, with the host matter. The charge species, such as α particles, β particles, and positrons, can be detected based on (i) the impact of these charge species/ions on the electric field (E) generated by the local environment or (ii) the light generated via radiative recombination, which is normally detected by scintillators. However, the information lost during this process due to photon–phonon interaction decreases the signal-to-noise ratio. To eliminate such losses, we can use nanoscintillators instead of single crystals because of the large reduction in phonon interaction in the nanodomain. This advantage of nanoscintillators significantly increases the signal-to-noise ratio because the charge carriers are detected due to low photon losses. Furthermore, low cost and large active area when compared with those of single crystals are other important reasons for designing nanostructured materials for scintillation applications.

Figure 21(a) shows the mixed α and γ energy spectrum emanating from a thin film with a ^{241}Am α particle source and ^{133}Ba γ-rays falling on a 1 cm × 1 cm detector. Based on pulse amplitude and the energy of occurrence, the type and quantity of radioactive source can be identified [202]. The pulse amplitudes of the full-energy γ-ray peaks from ^{133}Ba are linearly correlated with the energies identified from Fig. 21(b). The areas under the γ energy peaks correspond to the expected values. The areas under the 383.85-keV γ peaks should be 12% of those under the 356.02-keV peaks. This value is comparable with the measured value of 11% when considering the γ-ray emission yield and photoelectric absorption probabilities. If the detectors are considerably thick, the magnitudes of the escaped X-rays become negligible. Because the phonon losses will become minimal, it is better to work with thin detectors to detect charged species.

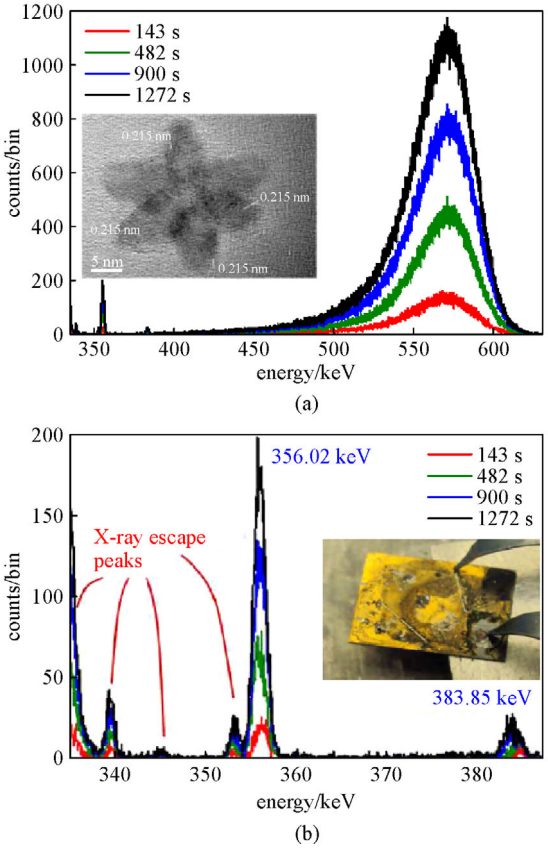

Fig. 21 (a) γ and α energy spectra derived from the ^{133}Ba and ^{241}Am isotopes, respectively, attenuated through 3.7-cm air by irradiating a 1 cm × 1 cm thin composite assembly of para-MEH–PPV and PbSe NPs. The spectra were obtained for various durations, as shown in the legend. The inset shows a TEM micrograph of PbSe NPs under assembly. (b) Typical ^{133}Ba spectra derived from a thin detector in which the Pb and Se X-ray escape peaks are prominent [202]

5.2 X-ray-induced photodynamic therapy (XPDT)

Scintillating nanomaterials can be easily combined with a photosensitizer for achieving efficient photodynamic therapy (PDT) [93,206–209]. Efficient photon energy transfer can be obtained from the nanoscintillators to the photosensitizer because of the broad spectral overlap between the emission of the former and the excitation of the latter. This process provides an additional advantage to enhance the efficacy during radiotherapy without any additional radiation dose. Yu et al. explored $Gd_2(WO_4)_3$:Tb nanoscintillators for performing XPDT [210]. Another group used $LiLuF_4$:Ce@SiO_2@Ag_3PO_4@Pt(IV) NPs and the electron acceptor Pt(IV) to improve the hydroxyl yield by increasing the distance between electrons and holes in the photosensitizer Ag_3PO_4 [211]. Bekah et al. explored LaF_3 NPs for performing XPDT by co-conjugating them with poly(ethylene glycol) and a photosensitizer [212]. Moreover, Alves et al. tabulated various nanoscintillators and photosensitizers that have been used for XPDT (Table 2) [108].

During the XPDT process, upon irradiation with X- or γ-rays, the nanoscintillators accumulated in a tumor cell serve as an internal light source to activate photosensitizers. Cytotoxic singlet oxygen is formed in case of cancerous tumors, killing cancerous cells. The synergistic effects of radiotherapy and PDT improve the treatment

Table 2 Different nanoscintillators exploited for XPDT [108]. Copyright 2018. Reproduced with permission from Impact Journals, LLC

year	nanoparticle	size	nanoparticle concentration	photosensitizer	X-ray energy	biological model
2008	$LaF_3:Tb^{3+}$	15 nm	0.035 M*	meso-tetra (4-carboxyphenyl) porphine (MTCP)	120 keV	N/A
2010	ZnO nanorods (NRs)	0.5 μm	N/A	protoporphyrin dimethyl ester (PPDME)	N/A	T47D cells
2011	Y_2O_3	12 nm	2.5–95 μg/mL	psoralen	2 Gy, 160 or 320 kVp	PC3 cells
2011	$Gd_2O_2S:Tb$	20 μm	5 mg/mL	photofrin II	120 keV, 20 mAs	human glioblastoma cells
2013	Tb_2O_3	10 nm	1 mM	porphyrin	N/A	N/A
2013	ZnO	50 nm	0.3–0.6 μM	mesi-tetra (4-sulfonatophenyl) porphyrin (TSPP)	N/A	escherichia coli
2014	$LaF_3:Ce^{3+}$	2 μm	1 μg/mL	protoporphyrin IX (PPIX)	3 Gy	PC3 cells
2016	$Sr_2MgSi_2O_7:Eu^{2+}$, Dy^{3+}	273 nm	10 μg/mL	protoporphyrin IX (PPIX)	1–7 Gy	PC3
2014	Cu–Cy	50–100 nm	50 μg	self	5 Gy	MCF-7 Xenograft
2016	AnS:Cu, Co	4 nm	0.05 mM	tetrabromorhodamine-123 (TBrRh123)	2 Gy	PC3 cells
2015	$SrAl_2O_4:Eu^{2+}$	80 nm	50 μg/mL	merocyanine 540 (MC540)	0.5 Gy	U87MG Xenograft
2015	$LaF_3:Tb$	3–45 nm	N/A	rose bengal (RB)	2–10 keV	N/A
2015	$LaF_3:Tb$	3–45 nm	20 mg/mL	rose bengal (RB)	N/A	tumor model
2016	CeF_3	7–11 nm	0.1–0.9 μM	veterporfin (VP)	6 Gy, 8 keV, or 6 MeV	Panc-1
2015	$LiYF_4:Ce^{3+}$	34 nm	25–50 μg/mL	ZnO	8 Gy	HeLa cells
2015	SiC/SiO_x NWs	20 nm	50 μg/mL	porphyrin	2 Gy, 6 MV	A549 cells
2015	ZnO/SiO_3	98 nm	0.005–0.05 M	ZnO	200 kVp, 2 Gy	LNCaP and Du145 cells
2015	$GdEuC_{12}$ micelle	4.6 nm	500 μM	hypericin (Hyp)	5–40 keV	HeLa cells

Note: * 1 M = 1 mol/L

efficiency. This technique is highly selective toward tumor cells; thus, it has become a highly popular and globally accepted technique. Its low toxicity offers another advantage over radiation and chemotherapy. The exploitation of high-Z NPs enhances the cross section for X-ray absorption, mostly at low X-ray energies (< 100 keV). Thus, the X-ray dose near NPs is enhanced, which is known as radiosensitization [213].

Nanoscintillators can be exploited for visible-to-UV upconversion, which is useful for killing pathogenic microorganisms based on biocidal surface technologies and for microbial inactivation in drinking water. The scintillating NPs that are engineered in terms of their surface area, particle size, particle shape, energy level, defects, etc., can absorb visible light and emit highly energetic UV radiation. If the upconverted nanoscintillators are placed close to the external surfaces of a cancerous tissue, they can be used for cancer treatment. However, the cure depth is not deeper than the red-light penetration depth into tissues, which does not exceed 1 cm. Figure 22 schematically shows the steps involved in PDT, where nanoscintillators are coupled with photosensitizers, producing singlet oxygen via the X-ray irradiation of tumor cells [214].

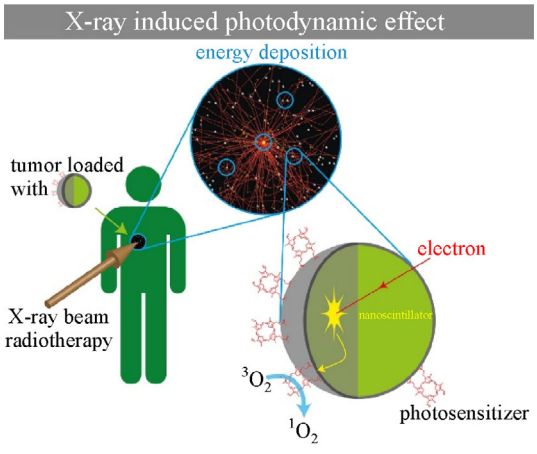

Fig. 22 Steps involved in the X-ray irradiation of tumors to produce singlet oxygen [214]. Copyright 2013. Reproduced with permission from the American Chemical Society

The principle of X-ray-excited scintillating NPs for performing PDT is presented in Fig. 23. X-ray-induced PDT is activated by the emitted visible light, which is used

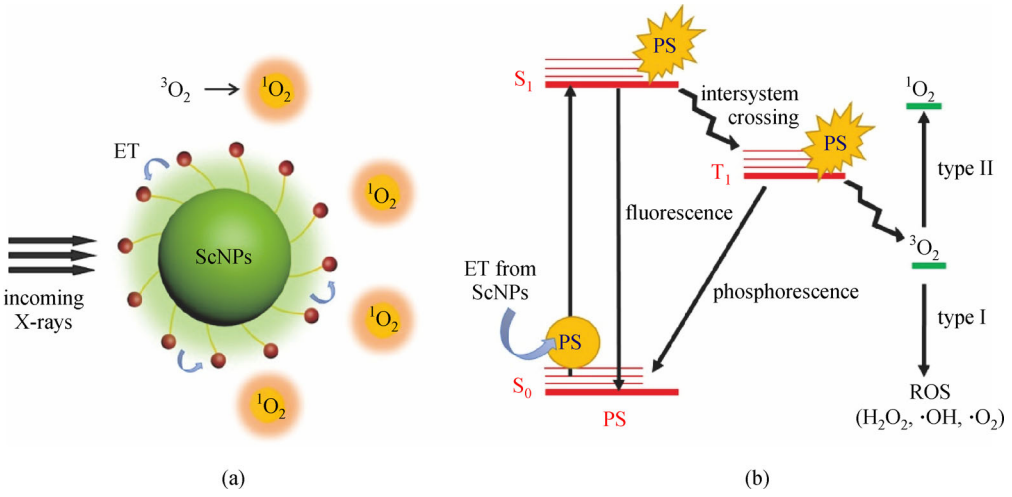

Fig. 23 (a) Scintillating NPs serve as an X-ray transducer to generate $^1O_2$ through the energy transfer process. (b) Diagram of the PDT mechanism that occurs when energy is transferred from the ScNPs to activate the PS. PS's electrons from the ground state (S_0) absorb energy and move to singlet-excited states (S_1) [1]. Copyright 2016. Reproduced with permission from the American chemical society

to activate the nearby photosensitizer. The promoted electron moves to a triplet excited state (T_1), and some of the absorbed energy is released via inter-system crossing. The triplet state has a relatively long half-life compared to singlet state. The released energy is allowed to be transferred to the nearby oxygen molecules. This generated oxygen ($^1O_2$) can damage the tumor cells in the surrounding area via the type-II pathway in majority of cases. The hosts inducing the conversion of X-rays to UV/Vis light for such applications are generally wide-bandgap materials. One picosecond is the timescale required for the conversion of X-ray energy. The conversion of a high-energy photon to a low-energy photon involves photo-electric and Compton scattering processes, which involve several photophysical steps during which many excitons are generated and thermalized in the CB and VB, respectively. When excitons are observed in the defect state in the bandgap of the host materials, nonradiative energy loss and other types of losses can be observed because of phonon interactions. The transportation of excitons is delayed in this process when the charge carriers get localized in the bandgap. The scintillation performance of a material can be significantly altered or degraded by various factors, including defects, surface energy, inter-stitials, and interfaces. The luminescence process during the final stage of scintillation comprises radiatively recombined electrons and holes at the luminescence center [13,80]. Simultaneously, the photon energy from the scintillator NPs will activate the nearest photosensitizer, causing $^1O_2$ generation, which is very toxic to cells.

Note

• The only difficulty associated with the exploitation of nanoscintillators is that their spectral profile deviates from that of the microcrystalline or single-crystal scintillators at times due to the modified crystal field [101]. This causes a substantial broadening of the emission peaks.

• In XPDT, majority of the X-ray photon energy is lost in the surrounding medium due to the small NP size relative to the range of the ionizing charged particles. Therefore, only a small fraction of X-ray energy is available to stimulate the nanoparticle luminescence [70].

5.3 X-ray luminescence computed tomography (XLCT) imaging

Morrone reported the usage of a scanning X-ray method to image optical emission from trivalent terbium-labeled actin in a single cell having a resolution of approximately 50 nm, which is considerably less than the far-field optical diffraction limit [215]. The X-ray-excited scintillating NPs, which can transfer photon energy to fluorescent photodynamic dyes, was demonstrated by Chen et al. [216–218]. They suggested that similar X-ray scintillator/fluorescent particles could serve as oxygen dosimeters [219]. Pratx et al. used X-ray luminescence computed tomography (XLCT) to detect the presence and location of X-ray phosphors in an optically diffusive medium [220]. Based on the selective excitation of 50-nm phosphors with a radiation dose of 1–100 cGy, a spatial resolution of 1 mm was achieved via the usage of tissue-mimicking materials and the optical detection of their luminescence [220]. Moreover, Pratx et al. showed that XLCT could image the cross-sectional distribution of micro-sized phosphor particles in a 1-cm agar tissue phantom [221].

During XLCT, the nanophosphors excited by X-rays emit near-infrared radiation based on the poor scattering of X-ray by the tissue cells inside the body. Therefore, high-contrast images can be obtained despite optical scattering

[220–222]. The usage of X-rays is advantageous because of their deeper penetration, negligible tissue autofluorescence background, and simpler image reconstruction approach [221]. Further modification of X-ray probes using targeted molecule and antibodies enhances XLCT's capability for deep tissue imaging.

Carbon nanotubes and QDs are some of the extensively explored nanomaterials that can be used for optical bioimaging [223–226]. However, there is serious concern about their efficiency due to their low QY, toxic nature, and size-dependent emission characteristics [227]. Recently, lanthanide-doped NPs have shown great potential for bioimaging, particularly in the shortwave infrared region [228]. Gd_2O_2S:Tb and CsI:Tl are the most widely explored scintillation materials for performing indirect digital X-ray imaging detection [229]. The final X-ray images are deteriorated owing to poor spatial resolution because the granular-type Gd_2O_2S:Tb included in scintillator screens has an average size of 5–10 micron; therefore, the light output generated with respect to the incident X-ray is scattered. Without the photon scattering of light, a high spatial resolution has been reported when using nanoscintillators [230,231]. Figure 24 shows the schematic of X-ray-excited optical luminescence used for X-ray imaging.

Core–shell NPs are the most favored systems, which exhibit several benefits such as high photostability, optical tunability with Stokes shifts of more than 100 nm, and intense and bright shortwave IR region luminescence [227]. Figure 25 shows the bright shortwave IR luminescence obtained using $NaYF_4$:Yb,Er core–shell nanoscintillators, which were exploited for bioimaging, nanoparticle tracing, and lymphatic mapping.

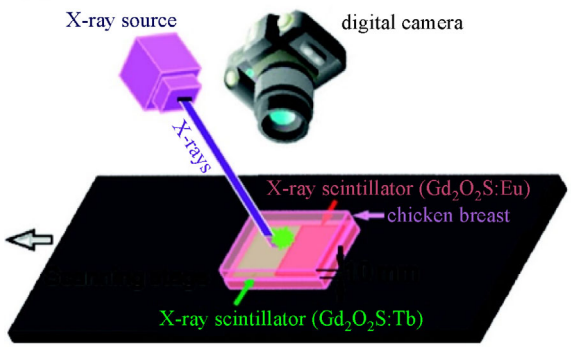

Fig. 24 Imaging of the X-ray-excited optical luminescence [232]. Copyright 2011. Reproduced with permission from the American chemical society

5.4 Microscopic diagnostics of biological and medical objects

Semiconductor QDs and nanoscintillators are the most extensively explored fluorescent sensors with respect to various biomolecules and their modifications [218,233–239]. They are highly sensitive luminescent markers and display obvious advantages compared to organic markers, including a wide range of excitation and emission spectra and high photobleaching resistance. Nanoscintillators can also be used in biochips for the *in vitro* detection of some specific organelles. The *in vivo* killing of cancerous cells and other pathological organelles inside an organism proceeds with the generation of cytotoxic singlet oxygen after X-ray excitation [154,162–168]. These

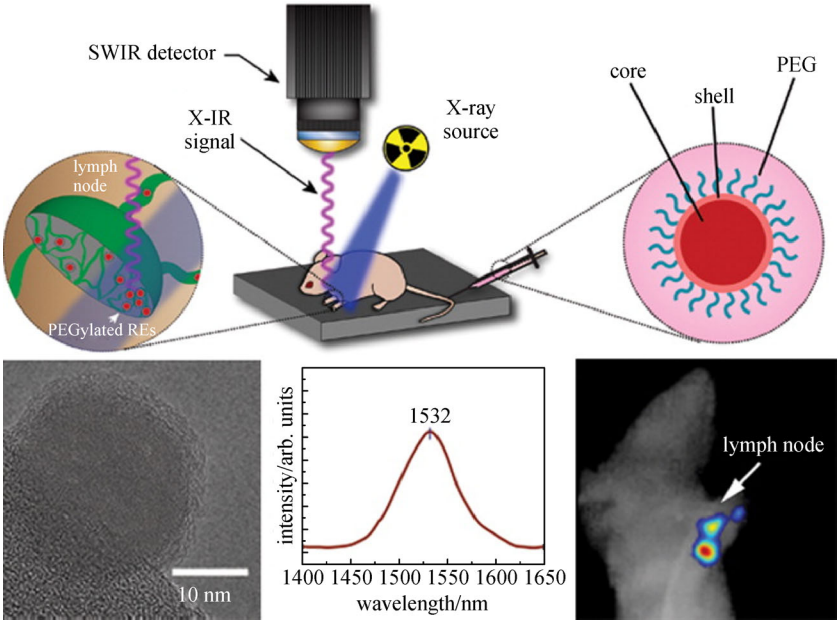

Fig. 25 Core–shell $NaYF_4$:Yb,Er nanoscintillator for X-ray induced shortwave IR luminescence in case of optical bioimaging [227]. Copyright 2015. Reproduced with permission from the American Chemical Society

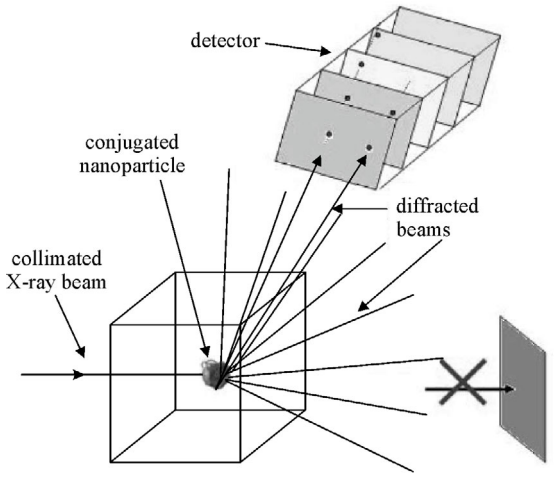

Fig. 26 X-ray detection of the pathological bio-objects bound to NPs [240]. Copyright 2009. Reproduced with permission from IEEE

pathological molecules are directly bonded with nanoscintillators or tagged using photosensitizers.

Some of the studied nanoscintillators demonstrated effective performance with respect to the aforementioned purposes. For example, due to their high density and effective atomic mass, the LuF_3 and LaF_3 nanoscintillators demonstrated high efficiency as X-ray absorbers and transferred the absorbed energy to the organic molecules conjugated with them [234,238,239]. Other important criteria for ensuring the effective biological performance of nanoscintillators include water solubility and easy introduction into tissues and blood. Special procedures have also been developed for improving the water solubility of inorganic NPs [238]. Figure 26 shows the schematic of the X-ray detection of the pathological bio-objects bound to NPs [240].

6 Outlook and conclusions

In this review article, we focused on the scintillation property of inorganic nanocrystals, their applications, and the advantages and disadvantages associated with their usage. We have also provided information about the fundamental principles and applications of scintillators in a nanosized domain. The types of ISs, their structures and applications, and the underlying scintillation mechanisms were also discussed. Nanocrystalline scintillator powder has been employed in a wide range of scientific and technological applications in various fields, including X-ray detection/dosimetry, biomedical imaging, and drug delivery-activation systems. Further, new challenges associated with the fabrication of high-performance nanoscintillators were discussed based on their structure, surface area, quantum confinement, and dielectric confinement. Because the surface defects of NPs provide nonradiative pathways and drastically decrease the RL efficiency, core–shell and coating strategies have been investigated to improve the scintillation efficiency. Discussions were also conducted to compare the scintillation performances of single crystals and ceramics. Furthermore, a concise picture of the current scenario in this growing field of optoelectronics was provided, and their advantages and disadvantages were discussed.

The scintillation properties were presented, and the effects of quantum and dielectric confinements on the performance of bulk and nanoscintillators were discussed. Suitable examples were provided to give a clear picture of the photophysical phenomena occurring in the nanosized domain. The basic phenomena governing the scintillation properties in the quantum and weak confinement zones were explained. Bandgap engineering was explained with respect to the concept of dielectric confinement.

The unique aspect of the scintillation process is that it is correlated with the migration of carriers through scintillators. The selection of hosts and dopants plays a critical role in determining the efficiency of the conversion and luminescence processes. By considering oxides, fluorides, clusters, and organic/inorganic compasites (OICs) as examples, the effects of hosts on the scintillation properties were explained. This mechanism was explained and thoroughly reviewed with respect to cluster compounds and MOFs for detecting ionizing radiation, including X-rays and γ-rays. Additional emphasis was given to explain the comparison of the performances of hafnium- and zirconium-based MOFs. OICs have emerged as smart materials and possess the properties of both inorganic and organic components, thereby exhibiting interesting scintillation properties. They display exceptional scintillation efficiency and are currently in high demand in fields of fundamental and applied research. The diverse properties of the existing materials were used to generate hybrid composite materials.

Scintillators can also be designed in various physical forms, including nanoparticles, ceramics, thin films, and GCs. Each form has its own advantages and disadvantages. The luminescence intensity of NPs is determined by their surface area, shape, and average size, the mean free path of the photoelectrons formed via X-ray absorption, and the thermalization length of the electrons. Powder phosphors and conventional single crystals have various distinct advantages compared to thin-film scintillators. Thick scintillators are not desirable for usage in RLM applications. Light is emitted throughout the track; therefore, it is difficult to localize the particle origin. Thin-film scintillators are advantageous for RLM, where light only emanates from the active volume of the scintillators located close to the cells. Even though the traditional ceramics comprise single or multiple crystalline and amorphous phases, they are normally translucent or opaque to light. Modern and technologically advanced OTCs are highly dense mono-

liths of the micro/nanosized crystals. The scintillators formed from crystals having cubic-structured OTCs are superior when compared with single crystals and exhibit ruggedness and glass processability. The performance of glass scintillators over single crystals is also presented. GCs are another class of scintillators that have been extensively explored because of their controllable properties and the desirable characteristics of glasses and sintered ceramics. The glass-ceramic synthesis routes allow considerable compositional flexibility and may be used to obtain crystallites of compounds that do not melt congruently in contrast to single crystals. We also reviewed the applications of nanostructured and bulk scintillators in various domains of scientific and technological detections, including ionizing radiation detectors, X-ray imaging sensors, microscopic diagnostics of biological and medical objects, nuclear medical imaging, and PDT. Thus, we comprehensively discussed scintillators from various perspectives, ranging from their fundamental principles to applications.

In the scientific and technological research domains, novel methods are being increasingly introduced with respect to the synthesis and applications of materials. The exploration of cost-efficient and sensitive materials is being prioritized to achieve improvements over the current detectors in case of ionizing radiation such as γ-rays and X-rays. NPs have shown considerable potential because the phonon-assisted loss processes can be suppressed to a larger degree in the nanodomain when compared with those in single crystals, which could be highly beneficial with respect to PL and scintillation. However, bulk scintillators have other advantages, including high optical transparency, large detection capability, and high energy resolution.

To enable synergistic co-treatment, dense inorganic NPs show unique dose enhancement properties in case of radiation therapy. The problems associated with tissues during PDT can be solved using dose enhancement induced by NPs and host-sensitized energy transfer from nanoscintillators to the photosensitizer molecules. Moreover, tailoring NPs for novel therapies, such as the combination of radiation and PDT, is gaining interest. With respect to the medical applications of scintillators, it becomes imperative to combine information obtained based on the theoretical and physical principles to obtain quantitative estimates for the expected efficacy under a range of physical parameters.

Many groups, including our research group, have worked extensively to develop an efficient nanoceramic powder for the aforementioned applications with reasonable success. In case of nanoscintillators, the feasibility of replacing the currently used materials is still being performed by many research groups. Because of the several studies performed globally and the associated positive results, we cannot ignore the superiority of nanomaterials over their bulk counterparts for applications in radiation detection, PDT, and bioimaging.

Furthermore, NPs seem to be the most efficient, easy, and feasible methodology to improve the delivery of water-insoluble photosensitizers for performing PDT. On the other hand, semiconductor QDs have been observed to be highly beneficial for the direct generation of singlet oxygen and for exciting the attached photosensitizer molecules. Progress on nanoparticle-assisted medical therapies has been achieved; however, there is still scope for much progress on nanoparticle radiosensitization effect. The underlying principles and interaction mechanisms will help to establish the role of nanoscintillators in medical fields where clinical applications have just started to emerge.

Acknowledgements SKG would like to thank the United States-India Education Foundation (USIEF, India) and the Institute of International Education (IIE, USA) for his Fulbright Nehru Postdoctoral Fellowship (Award# 2268/FNPDR/2017). YM thanks the financial support provided by the IIT startup funds.

References

1. Kamkaew A, Chen F, Zhan Y, Majewski R L, Cai W. Scintillating nanoparticles as energy mediators for enhanced photodynamic therapy. ACS Nano, 2016, 10(4): 3918–3935
2. Birowosuto M D, Cortecchia D, Drozdowski W, Brylew K, Lachmanski W, Bruno A, Soci C. X-ray scintillation in lead halide perovskite crystals. Scientific Reports, 2016, 6(1): 37254
3. Tsubota Y, Kaneko J H, Higuchi M, Nishiyama S, Ishibashi H. High-temperature scintillation properties of orthorhombic $Gd_2Si_2O_7$ aiming at well logging. Applied Physics Express, 2015, 8(6): 062602
4. Lecoq P. Development of new scintillators for medical applications. Nuclear Instruments & Methods in Physics Research. Section A, Accelerators, Spectrometers, Detectors and Associated Equipment, 2016, 809: 130–139
5. Jacobsohn L G, Sprinkle K B, Roberts S A, Kucera C J, James T L, Yukihara E G, DeVol T A, Ballato J. Fluoride nanoscintillators. Journal of Nanomaterials, 2011, 2011: 1
6. Rodnyi P A. Physical Processes in Inorganic Scintillators. Boca Raton: CRC Press, 1997
7. Lee S K, Kang S Y, Jang D Y, Lee C H, Kang S M. Comparison of new simple methods in fabricating ZnS (Ag) scintillators for detecting alpha particles. Nuclear science and technology, 2011, 1: 194–197
8. Knoll G F. Radiation Detection and Measurement. New York: John Wiley & Sons, 2010
9. Bizarri G. Scintillation mechanisms of inorganic materials: from crystal characteristics to scintillation properties. Journal of Crystal Growth, 2010, 312(8): 1213–1215
10. Shockley W. Problems related top-n junctions in silicon. Czechoslovak Journal of Physics, 1961, 11(2): 81–121
11. Robbins D. On predicting the maximum efficiency of phosphor systems excited by ionizing radiation. Journal of the Electro-

chemical Society, 1980, 127(12): 2694–2702
12. Blasse G. Search for new inorganic scintillators. IEEE Transactions on Nuclear Science, 1991, 38(1): 30–31
13. Blasse G. Scintillator materials. Chemistry of Materials, 1994, 6 (9): 1465–1475
14. Blasse G. Luminescent materials: is there still news? Journal of Alloys and Compounds, 1995, 225(1–2): 529–533
15. Derenzo S, Weber M, Bourret-Courchesne E, Klintenberg M. The quest for the ideal inorganic scintillator. Nuclear Instruments & Methods in Physics Research. Section A, Accelerators, Spectrometers, Detectors and Associated Equipment, 2003, 505(1–2): 111–117
16. Derenzo S E, Moses W, Cahoon J, Perera R, Litton J. Prospects for new inorganic scintillators. IEEE Transactions on Nuclear Science, 1990, 37(2): 203–208
17. Ishii M, Kobayashi M. Single crystals for radiation detectors. Progress in Crystal Growth and Characterization of Materials, 1992, 23: 245–311
18. Milbrath B D, Peurrung A J, Bliss M, Weber W J. Radiation detector materials: an overview. Journal of Materials Research, 2008, 23(10): 2561–2581
19. Liu C, Li Z, Hajagos T J, Kishpaugh D, Chen D Y, Pei Q. Transparent ultra-high-loading quantum dot/polymer nanocomposite monolith for gamma scintillation. ACS Nano, 2017, 11(6): 6422–6430
20. Heath R, Hofstadter R, Hughes E. Inorganic scintillators: a review of techniques and applications. Nuclear Instruments and Methods, 1979, 162(1–3): 431–476
21. Weber M J. Inorganic scintillators: today and tomorrow. Journal of Luminescence, 2002, 100(1–4): 35–45
22. Gupta T K. Characterization of Radiation Detectors (Scintillators) Used in Nuclear Medicine, Radiation, Ionization, and Detection in Nuclear Medicine. Berlin: Springer, 2013, 367–449
23. SyS C. Inorganic Scintillator Detectors. Available online via Caensys website
24. Lecoq P, Gektin A, Korzhik M. Influence of Crystal Structure Defects on Scintillation Properties. In: Inorganic Scintillators for Detector Systems. Particle Acceleration and Detection. Berlin: Springer, 2017, 197–252
25. Nikl M, Laguta V, Vedda A. Complex oxide scintillators: material defects and scintillation performance. Physica Status Solidi (B), 2008, 245: 1701–1722
26. Lisitsyn V, Lisitsyna L, Polisadova E. Complex defects in crystal scintillation materials and phosphors. IOP Conference Series. Materials Science and Engineering, 2017, 168: 012086
27. Kuklja M M. Defects in yttrium aluminium perovskite and garnet crystals: atomistic study. Journal of Physics Condensed Matter, 2000, 12(13): 2953–2967
28. Nikolopoulos D, Valais I, Michail C, Bakas A, Fountzoula C, Cantzos D, Bhattacharyya D, Sianoudis I, Fountos G, Yannakopoulos P, Panayiotakis G, Kandarakis I. Radioluminescence properties of the CdSe/ZnS quantum dot nanocrystals with analysis of long-memory trends. Radiation Measurements, 2016, 92: 19–31
29. Osakada Y, Pratx G, Sun C, Sakamoto M, Ahmad M, Volotskova O, Ong Q, Teranishi T, Harada Y, Xing L, Cui B. Hard X-ray-induced optical luminescence via biomolecule-directed metal clusters. Chemical Communications, 2014, 50(27): 3549–3551
30. Osakada Y, Pratx G, Hanson L, Solomon P E, Xing L, Cui B. X-ray excitable luminescent polymer dots doped with an iridium(III) complex. Chemical Communications, 2013, 49(39): 4319–4321
31. Wang C, Volotskova O, Lu K, Ahmad M, Sun C, Xing L, Lin W. Synergistic assembly of heavy metal clusters and luminescent organic bridging ligands in metal-organic frameworks for highly efficient X-ray scintillation. Journal of the American Chemical Society, 2014, 136(17): 6171–6174
32. Yaffe M J, Rowlands J A. X-ray detectors for digital radiography. Physics in Medicine and Biology, 1997, 42(1): 1–39
33. Gupta S K, Zuniga J P, Abdou M, Mao Y. Thermal annealing effects on $La_2Hf_2O_7:Eu^{3+}$ nanoparticles: a curious case study of structural evolution and site-specific photo- and radio-luminescence. Inorganic Chemistry Frontiers, 2018, 5(10): 2508–2521
34. Gupta S K, Zuniga J P, Ghosh P S, Abdou M, Mao Y. Correlating structure and luminescence properties of undoped and Eu^{3+}-doped $La_2Hf_2O_7$ nanoparticles prepared with different coprecipitating pH values through experimental and theoretical studies. Inorganic Chemistry, 2018, 57(18): 11815–11830
35. Pokhrel M, Gupta S K, Wahid K, Mao Y. Pyrochlore rare-earth hafnate $RE_2Hf_2O_7$ (RE = La and Pr) nanoparticles stabilized by molten-salt synthesis at low temperature. Inorganic Chemistry, 2019, 58(2): 1241–1251
36. Zuniga J P, Gupta S K, Pokhrel M, Mao Y. Exploring the optical properties of $La_2Hf_2O_7:Pr^{3+}$ nanoparticles under UV and X-ray excitation for potential lighting and scintillating applications. New Journal of Chemistry, 2018, 42(12): 9381–9392
37. Zuniga J P, Gupta S K, Abdou M, Mao Y. Effect of molten salt synthesis processing duration on the photo- and radioluminescence of UV-, visible-, and X-ray-excitable $La_2Hf_2O_7:Eu^{3+}$ nanoparticles. ACS Omega, 2018, 3(7): 7757–7770
38. Pokhrel M, Alcoutlabi M, Mao Y. Optical and X-ray induced luminescence from Eu^{3+} doped $La_2Zr_2O_7$ nanoparticles. Journal of Alloys and Compounds, 2017, 693: 719–729
39. Pokhrel M, Burger A, Groza M, Mao Y. Enhance the photoluminescence and radioluminescence of $La_2Zr_2O_7:Eu^{3+}$ core nanoparticles by coating with a thin Y_2O_3 shell. Optical Materials, 2017, 68: 35–41
40. Wahid K, Pokhrel M, Mao Y. Structural, photoluminescence and radioluminescence properties of Eu^{3+} doped $La_2Hf_2O_7$ nanoparticles. Journal of Solid State Chemistry, 2017, 245: 89–97
41. Gupta S K, Abdou M, Ghosh P S, Zuniga J P, Mao Y. Thermally induced disorder-order phase transition of $Gd_2Hf_2O_7:Eu^{3+}$ nanoparticles and its implication on photo- and radioluminescence. ACS Omega, 2019, 4(2): 2779–2791
42. Gupta S K, Abdou M, Zuniga J P, Ghosh P S, Molina E, Xu B, Chipara M, Mao Y. Roles of oxygen vacancies and pH induced size changes on photo- and radioluminescence of undoped and Eu^{3+}-doped $La_2Zr_2O_7$ nanoparticles. Journal of Luminescence, 2019, 209: 302–315
43. Abdou M, Gupta S K, Zuniga J P, Mao Y. On structure and phase transformation of uranium doped $La_2Hf_2O_7$ nanoparticles as an efficient nuclear waste host. Materials Chemistry Frontiers, 2018, 2

(12): 2201–2211
44. Gupta S K, Abdou M, Zuniga J P, Puretzky A A, Mao Y. Samarium-activated $La_2Hf_2O_7$ nanoparticles as multifunctional phosphors. ACS Omega, 2019, 4(19): 17956–17966
45. Gupta S K, Zuniga J P, Abdou M, Ghosh P S, Mao Y. Optical properties of undoped, Eu^{3+} doped and Li^{+} co-doped $Y_2Hf_2O_7$ nanoparticles and polymer nanocomposite films. Inorganic Chemistry Frontiers, 2020, 7(2): 505–518
46. Zuniga J P, Gupta S K, Abdou M, De Santiago H A, Puretzky A A, Thomas M P, Guiton B S, Liu J, Mao Y. Size, structure, and luminescence of $Nd_2Zr_2O_7$ nanoparticles by molten salt synthesis. Journal of Materials Science, 2019, 54(19): 12411–12423
47. Abdou M, Gupta S K, Zuniga J P, Mao Y. Insight into the effect of A-site cations on structural and optical properties of $RE_2Hf_2O_7$:U nanoparticles. Journal of Luminescence, 2019, 210: 425–434
48. Gupta S K, Penilla Garcia M A, Zuniga J P, Abdou M, Mao Y. Visible and ultraviolet upconversion and near infrared down-conversion luminescence from lanthanide doped $La_2Zr_2O_7$ nanoparticles. Journal of Luminescence, 2019, 214: 116591
49. Gupta S K, Zuniga J P, Abdou M, Thomas M P, De Alwis Goonatilleke M, Guiton B S, Mao Y. Lanthanide-doped lanthanum hafnate nanoparticles as multicolor phosphors for warm white lighting and scintillators. Chemical Engineering Journal, 2020, 379: 122314
50. Penilla Garcia M A, Gupta S K, Mao Y. Effects of molten-salt processing parameters on the structural and optical properties of preformed $La_2Zr_2O_7$:Eu^{3+} nanoparticles. Ceramics International, 2020, 46(2): 1352–1361
51. Jagtap S, Chopade P, Tadepalli S, Bhalerao A, Gosavi S. A review on the progress of ZnSe as inorganic scintillator. Opto-Electronics Review, 2019, 27(1): 90–103
52. Chen Q, Wu J, Ou X, Huang B, Almutlaq J, Zhumekenov A A, Guan X, Han S, Liang L, Yi Z, Li J, Xie X, Wang Y, Li Y, Fan D, Teh D B L, All A H, Mohammed O F, Bakr O M, Wu T, Bettinelli M, Yang H, Huang W, Liu X. All-inorganic perovskite nanocrystal scintillators. Nature, 2018, 561(7721): 88–93
53. Pan W, Wu H, Luo J, Deng Z, Ge C, Chen C, Jiang X, Yin W J, Niu G, Zhu L, Yin L, Zhou Y, Xie Q, Ke X, Sui M, Tang J. Cs_2AgBiB_6 single-crystal X-ray detectors with a low detection limit. Nature Photonics, 2017, 11(11): 726–732
54. Zhang Y, Sun R, Ou X, Fu K, Chen Q, Ding Y, Xu L J, Liu L, Han Y, Malko A V, Liu X, Yang H, Bakr O M, Liu H, Mohammed O F. Metal halide perovskite nanosheet for X-ray high-resolution scintillation imaging screens. ACS Nano, 2019, 13(2): 2520–2525
55. Fu H. Review of lead-free halide perovskites as light-absorbers for photovoltaic applications: from materials to solar cells. Solar Energy Materials and Solar Cells, 2019, 193: 107–132
56. Wang X, Zhang T, Lou Y, Zhao Y. All-inorganic lead-free perovskites for optoelectronic applications. Materials Chemistry Frontiers, 2019, 3(3): 365–375
57. Yamamoto S, Kamada K, Yoshikawa A. Ultrahigh resolution radiation imaging system using an optical fiber structure scintillator plate. Scientific Reports, 2018, 8(1): 3194
58. Berneking A, Gola A, Ferri A, Finster F, Rucatti D, Paternoster G, Shah N J, Piemonte C, Lerche C. A new PET detector concept for compact preclinical high-resolution hybrid MR-PET. Nuclear Instruments & Methods in Physics Research. Section A, Accelerators, Spectrometers, Detectors and Associated Equipment, 2018, 888: 44–52
59. Hsu C C, Lin S L, Chang C A. Lanthanide-doped core-shell-shell nanocomposite for dual photodynamic therapy and luminescence imaging by a single X-ray excitation source. ACS Applied Materials & Interfaces, 2018, 10(9): 7859–7870
60. Li X, Xue Z, Jiang M, Li Y, Zeng S, Liu H. Soft X-ray activated $NaYF_4$:Gd/Tb scintillating nanorods for *in vivo* dual-modal X-ray/X-ray-induced optical bioimaging. Nanoscale, 2018, 10(1): 342–350
61. Hu C, Zhang L, Zhu R Y, Chen A, Wang Z, Ying L, Yu Z. Ultrafast inorganic scintillators for GHz hard X-Ray imaging. IEEE Transactions on Nuclear Science, 2018, 65(8): 2097–2104
62. Miller S R, Bhandari H B, Bhattacharya P, Brecher C, Crespi J, Couture A, Dinca C, Rommel M, Nagarkar V V. Reduced afterglow codoped CsI:Tl for high energy imaging. IEEE Transactions on Nuclear Science, 2018, 65(8): 2105–2108
63. Blasse G, Grabmaier B. Luminescent Materials. Berlin: Springer Science & Business Media, 2012
64. Grabmaier B, Rossner W, Leppert J. Ceramic scintillators for X-Ray computed tomography. Physica Status Solidi (A), 1992, 130: K183–K187
65. Greskovich C, Duclos S. Ceramic scintillators. Annual Review of Materials Science, 1997, 27(1): 69–88
66. Buşe G, Giuliani A, De Marcillac P, Marnieros S, Nones C, Novati V, Olivieri E, Poda D, Redon T, Sand J B, Veber P, Velázquez M, Zolotarova A S. First scintillating bolometer tests of a CLYMENE R&D on Li_2MoO_4 scintillators towards a large-scale double-beta decay experiment. Nuclear Instruments and Methods in Physics Research Section A: Accelerators, Spectrometers, Detectors and Associated Equipment, 2018, 891: 87–91
67. Zhu M, Qi H, Pan M, Hou Q, Jiang B, Jin Y, Han H, Song Z, Zhang H. Growth and luminescent properties of Yb:YAG and Ca co-doped Yb:YAG ultrafast scintillation crystals. Journal of Crystal Growth, 2018, 490: 51–55
68. Khan A, Rooh G, Kim H, Kim S. Ce^{3+}-activated Tl_2GdCl_5: novel halide scintillator for X-ray and γ-ray detection. Journal of Alloys and Compounds, 2018, 741: 878–882
69. Jung J, Hirata G, Gundiah G, Derenzo S, Wrasidlo W, Kesari S, Makale M, McKittrick J. Identification and development of nanoscintillators for biotechnology applications. Journal of Luminescence, 2014, 154: 569–577
70. Klein J S, Sun C, Pratx G. Radioluminescence in biomedicine: physics, applications, and models. Physics in Medicine and Biology, 2019, 64(4): 04TR01
71. Growing Single Crystals. In: Carter C B, Norton M G, eds. Ceramic Materials: Science and Engineering. New York: Springer, 2007, 507–526
72. Savytskii D, Knorr B, Dierolf V, Jain H. Demonstration of single crystal growth via solid-solid transformation of a glass. Scientific Reports, 2016, 6(1): 23324
73. Kivambe M, Aissa B, Tabet N. Emerging technologies in crystal growth of photovoltaic silicon: progress and challenges. Energy Procedia, 2017, 130: 7–13
74. Zhang C, Lin J. Defect-related luminescent materials: synthesis,

emission properties and applications. Chemical Society Reviews, 2012, 41(23): 7938–7961
75. Persyk D E, Schardt M A, Moi T E, Ritter K A, Muehllehner G. Research on pure sodium iodide as a practical scintillator. IEEE Transactions on Nuclear Science, 1980, 27(1): 167–171
76. Andryushchenko L, Grinev B, Udovichenko L, Litichevsky A. Improved NaI(Tl) scintillation detectors. Instruments and Experimental Techniques, 1997, 40: 59–63
77. Verger L, Ouvrier-Buffet P, Mathy F, Montemont G, Picone M, Rustique J, Riffard C. Performance of a new CdZnTe portable spectrometric system for high energy applications. IEEE Transactions on Nuclear Science, 2005, 52(5): 1733–1738
78. Berninger W. Monolithic gamma detector arrays and position sensitive detectors in high purity germanium. IEEE Transactions on Nuclear Science, 1974, 21(1): 374–378
79. Milbrath B D, Peurrung A J, Bliss M, Weber W J. Radiation detector materials: an overview. Journal of Materials Research, 2008, 23(10): 2561–2581
80. Nikl M. Scintillation detectors for X-rays. Measurement Science & Technology, 2006, 17(4): R37–R54
81. Greskovich C, Duclos S. Ceramic scinitillators. Annual Review of Materials Science, 1997, 27(1): 69–88
82. Jung J Y, Hirata G A, Gundiah G, Derenzo S, Wrasidlo W, Kesari S, Makale M T, McKittrick J. Identification and development of nanoscintillators for biotechnology applications. Journal of Luminescence, 2014, 154: 569–577
83. Brown S S, Rondinone A J, Dai S. Applications of Nanoparticles in Scintillation Detectors. Washington: ACS Publications, 2007
84. Liu C, Li Z, Hajagos T J, Kishpaugh D, Chen D Y, Pei Q. Transparent ultra-high-loading quantum dot/polymer nanocomposite monolith for gamma scintillation. ACS Nano, 2017, 11(6): 6422–6430
85. Yildirim S, Asal E C K, Ertekin K, Celik E. Luminescent properties of scintillator nanophosphors produced by flame spray pyrolysis. Journal of Luminescence, 2017, 187: 304–312
86. Hernandez-Sanchez B A, Boyle T J, Villone J, Yang P, Kinnan M, Hoppe S, Thoma S, Hattar K M, Doty F P. Size effects on the properties of high Z scintillator materials. In: Proceedings of Penetrating Radiation Systems and Applications XIII, International Society for Optics and Photonics, 2012, 85090G
87. Stouwdam J W, van Veggel F C. Improvement in the luminescence properties and processability of LaF_3/Ln and $LaPO_4$/Ln nanoparticles by surface modification. Langmuir, 2004, 20(26): 11763–11771
88. Kömpe K, Lehmann O, Haase M. Spectroscopic distinction of surface and volume ions in cerium (III)-and terbium (III)-containing core and core/shell nanoparticles. Chemistry of Materials, 2006, 18(18): 4442–4446
89. Cooke D, Lee J K, Bennett B, Groves J, Jacobsohn L, McKigney E, Muenchausen R, Nastasi M, Sickafus K, Tang M, Valdez J A, Kim J Y, Hong K S. Luminescent properties and reduced dimensional behavior of hydrothermally prepared Y_2SiO_5:Ce nanophosphors. Applied Physics Letters, 2006, 88(10): 103108
90. Muenchausen R, Jacobsohn L, Bennett B, McKigney E, Smith J, Cooke D. A novel method for extracting oscillator strength of select rare-earth ion optical transitions in nanostructured dielectric materials. Solid State Communications, 2006, 139(10): 497–500
91. Kyung Cha B, Jun Lee S, Muralidharan P, Yul Kim J, Kim D K, Cho G. Characterization and imaging performance of nanoscintillator screen for high resolution X-ray imaging detectors. Nuclear Instruments & Methods in Physics Research. Section A, Accelerators, Spectrometers, Detectors and Associated Equipment, 2011, 633: S294–S296
92. Klassen N V, Kedrov V V, Ossipyan Y A, Shmurak S Z, Shmyt Ko I M, Krivko O A, Kudrenko E A, Kurlov V N, Kobelev N P, Kiselev A P, Bozhko S I. Nanoscintillators for microscopic diagnostics of biological and medical objects and medical therapy. IEEE Transactions on Nanobioscience, 2009, 8(1): 20–32
93. Scaffidi J P, Gregas M K, Lauly B, Zhang Y, Vo-Dinh T. Activity of psoralen-functionalized nanoscintillators against cancer cells upon X-ray excitation. ACS Nano, 2011, 5(6): 4679–4687
94. Roy I, Ohulchanskyy T Y, Pudavar H E, Bergey E J, Oseroff A R, Morgan J, Dougherty T J, Prasad P N. Ceramic-based nanoparticles entrapping water-insoluble photosensitizing anticancer drugs: a novel drug-carrier system for photodynamic therapy. Journal of the American Chemical Society, 2003, 125(26): 7860–7865
95. Guss P, Guise R, Yuan D, Mukhopadhyay S, O'Brien R, Lowe D, Kang Z, Menkara H, Nagarkar V V. Lanthanum halide nanoparticle scintillators for nuclear radiation detection. Journal of Applied Physics, 2013, 113(6): 064303
96. Walters R J, Kalkman J, Polman A, Atwater H A, de Dood M J A. Photoluminescence quantum efficiency of dense silicon nanocrystal ensembles in SiO_2. Physical Review B, 2006, 73(13): 132302
97. Balazs A C, Emrick T, Russell T P. Nanoparticle polymer composites: where two small worlds meet. Science, 2006, 314 (5802): 1107–1110
98. Létant S E, Wang T F. Semiconductor quantum dot scintillation under γ-ray irradiation. Nano Letters, 2006, 6(12): 2877–2880
99. Liu C. High-Z nanoparticle/polymer nanocomposites for gamma-ray scintillation detectors. Dissertation for the Doctoral Degree. Los Angeles: University of California, 2017
100. Novak B M. Hybrid nanocomposite materials—between inorganic glasses and organic polymers. Advanced Materials, 1993, 5(6): 422–433
101. Dujardin C, Amans D, Belsky A, Chaput F, Ledoux G, Pillonnet A. Luminescence and scintillation properties at the nanoscale. IEEE Transactions on Nuclear Science, 2010, 57(3): 1348–1354
102. Braverman J B, Fabris L, Newby J, Hornback D, Ziock K P. Three-dimensional event localization in bulk scintillator crystals using optical coded apertures. In: Proceedings of IEEE Nuclear Science Symposium and Medical Imaging Conference (NSS/MIC), 2014, 1–8
103. Braverman J B. Event localization in bulk scintillator crystals using optical coded apertures. Dissertation for the Doctoral Degree. Knoxville: University of Tennessee, 2015
104. Melcher C. Perspectives on the future development of new scintillators. Nuclear Instruments & Methods in Physics Research. Section A, Accelerators, Spectrometers, Detectors and Associated Equipment, 2005, 537(1–2): 6–14
105. Taheri A, Saramad S, Setayeshi S. Geant4 simulation of zinc oxide nanowires in anodized aluminum oxide template as a low energy

X-ray scintillator detector. Nuclear Instruments & Methods in Physics Research. Section A, Accelerators, Spectrometers, Detectors and Associated Equipment, 2013, 701: 30–36

106. Taheri A, Saramad S, Ghalenoei S, Setayeshi S. Taheri-Saramad X-ray detector (TSXD): a novel high spatial resolution X-ray imager based on ZnO nano scintillator wires in polycarbonate membrane. Review of Scientific Instruments, 2014, 85(1): 013112
107. Ashworth C. Super scintillators. Nature Reviews. Materials, 2018, 3(10): 355
108. Alves L A, Ferreira L B, Pacheco P F, Mendivelso E A C, Teixeira P C N, Faria R X. Pore forming channels as a drug delivery system for photodynamic therapy in cancer associated with nanoscintillators. Oncotarget, 2018, 9(38): 25342–25354
109. Winterer M, Nitsche R, Hahn H. Local structure in nanocrystalline ZrO_2 and Y_2O_3 by EXAFS. Nanostructured Materials, 1997, 9(1–8): 397–400
110. Nigam S, Sudarsan V, Majumder C, Vatsa R. Structural differences existing in bulk and nanoparticles of $Y_2Sn_2O_7$: investigated by experimental and theoretical methods. Journal of Solid State Chemistry, 2013, 200: 202–208
111. Cutler P A. Synthesis and scintillation of single crystal and polycrystalline rare-earth-activated lutetium aluminum garnet. Dissertation for the Master Degree. Knoxville: University of Tennessee, 2010
112. Ryskin N N, Dorenbos P, Eijk C W E, Batygov S K. Scintillation properties of $Lu_3Al_{5-x}Sc_xO_{12}$ crystals. Journal of Physics Condensed Matter, 1994, 6(47): 10423–10434
113. Zhuravleva M, Yang K, Spurrier-Koschan M, Szupryczynski P, Yoshikawa A, Melcher C. Crystal growth and characterization of LuAG:Ce:Tb scintillator. Journal of Crystal Growth, 2010, 312(8): 1244–1248
114. Edgar A, Bartle M, Varoy C, Raymond S, Williams G. Structure and scintillation properties of cerium-doped barium chloride ceramics: effects of cation and anion substitution. IEEE Transactions on Nuclear Science, 2010, 57(3): 1218–1222
115. Peng X, Schlamp M C, Kadavanich A V, Alivisatos A P. Epitaxial growth of highly luminescent CdSe/CdS core/shell nanocrystals with photostability and electronic accessibility. Journal of the American Chemical Society, 1997, 119(30): 7019–7029
116. Ledoux G, Gong J, Huisken F. Effect of passivation and aging on the photoluminescence of silicon nanocrystals. Applied Physics Letters, 2001, 79(24): 4028–4030
117. Huignard A, Buissette V, Franville A C, Gacoin T, Boilot J P. Emission processes in YVO_4:Eu nanoparticles. Journal of Physical Chemistry B, 2003, 107(28): 6754–6759
118. Wang F, Wang J, Liu X. Direct evidence of a surface quenching effect on size-dependent luminescence of upconversion nanoparticles. Angewandte Chemie, 2010, 49(41): 7456–7460
119. Han J, Hirata G, Talbot J, McKittrick J. Luminescence enhancement of Y_2O_3:Eu^{3+} and Y_2SiO_5:Ce^{3+},Tb^{3+} core particles with SiO_2 shells. Materials Science and Engineering B, 2011, 176(5): 436–441
120. Li G Z, Yu M, Wang Z L, Lin J, Wang R S, Fang J. Sol–gel fabrication and photoluminescence properties of SiO_2@Gd_2O_3:Eu^{3+} core-shell particles. Journal of Nanoscience and Nanotechnology, 2006, 6(5): 1416–1422
121. Bao A, Lai H, Yang Y, Liu Z, Tao C, Yang H. Luminescent properties of YVO_4:Eu/SiO_2 core–shell composite particles. Journal of Nanoparticle Research, 2010, 12(2): 635–643
122. Yu M, Wang H, Lin C, Li G, Lin J. Sol–gel synthesis and photoluminescence properties of spherical SiO_2@LaPO4:Ce^{3+}/Tb^{3+} particles with a core–shell structure. Nanotechnology, 2006, 17(13): 3245–3252
123. Osseni S A, Lechevallier S, Verelst M, Dujardin C, Dexpert-Ghys J, Neumeyer D, Leclercq M, Baaziz H, Cussac D, Santran V, Mauricot R. New nanoplatform based on Gd_2O_2S:Eu^{3+} core: synthesis, characterization and use for *in vitro* bio-labelling. Journal of Materials Chemistry, 2011, 21(45): 18365–18372
124. Ledoux G, Mercier B, Louis C, Dujardin C, Tillement O, Perriat P. Synthesis and optical characterization of Gd_2O_3:Eu^{3+} nanocrystals: surface states and VUV excitation. Radiation Measurements, 2004, 38(4–6): 763–766
125. Bol A A, Meijerink A. Luminescence quantum efficiency of nanocrystalline ZnS:Mn^{2+}. 1. Surface passivation and Mn^{2+} concentration. Journal of Physical Chemistry B, 2001, 105(42): 10197–10202
126. Pokhrel M, Burger A, Groza M, Mao Y. Enhance the photoluminescence and radioluminescence of $La_2Zr_2O_7$:Eu^{3+} core nanoparticles by coating with a thin Y_2O_3 shell. Optical Materials, 2017, 68: 35–41
127. Holloway P H, Davidson M, Jacobsohn L G. Strategy for enhanced light output from luminescent nanoparticles. Technical report. Gainesville: Florida University, 2013
128. Jacobsohn L, Kucera C, Sprinkle K, Roberts S, Yukihara E, DeVol T, Ballato J. Scintillation of nanoparticles: case study of rare earth doped fluorides. Nuclear Science Symposium Conference Record (NSS/MIC), IEEE, 2010, 1600–1602
129. Gupta S K, Sudarshan K, Ghosh P, Sanyal K, Srivastava A, Arya A, Pujari P, Kadam R. Luminescence of undoped and Eu^{3+} doped nanocrystalline $SrWO_4$ scheelite: time resolved fluorescence complimented by DFT and positron annihilation spectroscopic studies. RSC Advances, 2016, 6(5): 3792–3805
130. Gupta S K, Sudarshan K, Ghosh P, Srivastava A, Bevara S, Pujari P, Kadam R. Role of various defects in the photoluminescence characteristics of nanocrystalline $Nd_2Zr_2O_7$: an investigation through spectroscopic and DFT calculations. Journal of Materials Chemistry. C, Materials for Optical and Electronic Devices, 2016, 4(22): 4988–5000
131. Gupta S K, Sudarshan K, Srivastava A, Kadam R. Visible light emission from bulk and nano $SrWO_4$: possible role of defects in photoluminescence. Journal of Luminescence, 2017, 192: 1220–1226
132. Vetrone F, Boyer J C, Capobianco J A, Speghini A, Bettinelli M. Concentration-dependent near-infrared to visible upconversion in nanocrystalline and bulk Y_2O_3:Er^{3+}. Chemistry of Materials, 2003, 15(14): 2737–2743
133. Yang L, Li L, Zhao M, Li G. Size-induced variations in bulk/surface structures and their impact on photoluminescence properties of $GdVO_4$:Eu^{3+} nanoparticles. Physical Chemistry Chemical Physics, 2012, 14(28): 9956–9965

134. Jacobsohn L, Sprinkle K, Kucera C, James T, Roberts S, Qian H, Yukihara E, DeVol T, Ballato J. Synthesis, luminescence and scintillation of rare earth doped lanthanum fluoride nanoparticles. Optical Materials, 2010, 33(2): 136–140
135. Klassen N, Kedrov V, Kurlov V, Ossipyan Y A, Shmurak S, Shmyt'ko I, Strukova G, Kobelev N, Kudrenko E, Krivko O, Kiselev A P, Bazhenov A V, Fursova T N. Advantages and problems of nanocrystalline scintillators. IEEE Transactions on Nuclear Science, 2008, 55(3): 1536–1541
136. Cha B K, Lee S J, Muralidharan P, Kim J Y, Kim D K, Cho G. Characterization and imaging performance of nanoscintillator screen for high resolution X-ray imaging detectors. Nuclear Instruments & Methods in Physics Research. Section A, Accelerators, Spectrometers, Detectors and Associated Equipment, 2011, 633: S294–S296
137. Hiyama F, Noguchi T, Koshimizu M, Kishimoto S, Haruki R, Nishikido F, Yanagida T, Fujimoto Y, Aida T, Takami S, Adschiri T, Asai K. X-ray detection capabilities of plastic scintillators incorporated with hafnium oxide nanoparticles surface-modified with phenyl propionic acid. Japanese Journal of Applied Physics, 2018, 57(1): 012601
138. Reithmaier J P, Sęk G, Löffler A, Hofmann C, Kuhn S, Reitzenstein S, Keldysh L V, Kulakovskii V D, Reinecke T L, Forchel A. Strong coupling in a single quantum dot-semiconductor microcavity system. Nature, 2004, 432(7014): 197–200
139. Klassen N, Shmyt'ko I, Strukova G, Kedrov V, Kobelev N, Kudrenko E, Kiseliov A, Prokopiuk N. Improvement of scintillation parameters in complex oxides by formation of nanocrystalline structures. In: Proceedings of 8th International SCINT Conference, 2005, 228–231
140. Wilkinson J, Ucer K, Williams R. The oscillator strength of extended exciton states and possibility for very fast scintillators. Nuclear Instruments & Methods in Physics Research. Section A, Accelerators, Spectrometers, Detectors and Associated Equipment, 2005, 537(1–2): 66–70
141. Elliot R J, Loudon R. Theory of the absorption edge in semiconductors in a high magnetic field. Journal of Physics and Chemistry of Solids, 1960, 15: 196–207
142. Murray C, Norris D J, Bawendi M G. Synthesis and characterization of nearly monodisperse CdE (E = sulfur, selenium, tellurium) semiconductor nanocrystallites. Journal of the American Chemical Society, 1993, 115(19): 8706–8715
143. Milliron D J, Hughes S M, Cui Y, Manna L, Li J, Wang L W, Alivisatos A P. Colloidal nanocrystal heterostructures with linear and branched topology. Nature, 2004, 430(6996): 190–195
144. Costa-Fernández J M, Pereiro R, Sanz-Medel A. The use of luminescent quantum dots for optical sensing. Trends in Analytical Chemistry, 2006, 25(3): 207–218
145. Henini M, Bugajski M. Advances in self-assembled semiconductor quantum dot lasers. Microelectronics Journal, 2005, 36(11): 950–956
146. Létant S E, Wang T F. Semiconductor quantum dot scintillation under γ-ray irradiation. Nano Letters, 2006, 6(12): 2877–2880
147. Shibuya K, Koshimizu M, Murakami H, Muroya Y, Katsumura Y, Asai K. Development of ultra-fast semiconducting scintillators using quantum confinement effect. Japanese Journal of Applied Physics, 2004, 43(10B): L1333–L1336
148. Liu B, Wu Q, Zhu Z, Cheng C, Gu M, Xu J, Chen H, Liu J, Chen L, Zhang Z, Ouyang X. Directional emission of quantum dot scintillators controlled by photonic crystals. Applied Physics Letters, 2017, 111(8): 081904
149. Blasse G, Grabmaier B. Energy Transfer, Luminescent Materials. Berlin: Springer, 1994, 91–107
150. Wuister S F, de Mello Donega C, Meijerink A. Local-field effects on the spontaneous emission rate of CdTe and CdSe quantum dots in dielectric media. Journal of Chemical Physics, 2004, 121(9): 4310–4315
151. Lamouche G, Lavallard P, Gacoin T. Optical properties of dye molecules as a function of the surrounding dielectric medium. Physical Review A, 1999, 59(6): 4668–4674
152. Meltzer R, Feofilov S, Tissue B, Yuan H. Dependence of fluorescence lifetimes of Y_2O_3:Eu^{3+} nanoparticles on the surrounding medium. Physical Review B, 1999, 60(20): R14012–R14015
153. Dolgaleva K, Boyd R W, Milonni P W. Influence of local-field effects on the radiative lifetime of liquid suspensions of Nd:YAG nanoparticles. Journal of the Optical Society of America B, Optical Physics, 2007, 24(3): 516–521
154. Chon B, Lim S J, Kim W, Seo J, Kang H, Joo T, Hwang J, Shin S K. Shell and ligand-dependent blinking of CdSe-based core/shell nanocrystals. Physical Chemistry Chemical Physics, 2010, 12(32): 9312–9319
155. Li J G, Sakka Y. Recent progress in advanced optical materials based on gadolinium aluminate garnet ($Gd_3Al_5O_{12}$). Science and Technology of Advanced Materials, 2015, 16(1): 014902
156. Seeley Z M, Cherepy N J, Payne S A. Expanded phase stability of Gd-based garnet transparent ceramic scintillators. Journal of Materials Research, 2014, 29(19): 2332–2337
157. Nikl M, Kamada K, Babin V, Pejchal J, Pilarova K, Mihokova E, Beitlerova A, Bartosiewicz K, Kurosawa S, Yoshikawa A. Defect engineering in Ce-doped aluminum garnet single crystal scintillators. Crystal Growth & Design, 2014, 14(9): 4827–4833
158. Nikl M, Yoshikawa A, Kamada K, Nejezchleb K, Stanek C R, Mares J A, Blazek K. Development of LuAG-based scintillator crystals: a review. Progress in Crystal Growth and Characterization of Materials, 2013, 59(2): 47–72
159. Eagleman Y, Weber M, Chaudhry A, Derenzo S. Luminescence study of cerium-doped $La_2Hf_2O_7$: effects due to trivalent and tetravalent cerium and oxygen vacancies. Journal of Luminescence, 2012, 132(11): 2889–2896
160. Gupta S K, Zuniga J P, Ghosh P S, Abdou M, Mao Y. Correlating structure and luminescence properties of undoped and $La_2Hf_2O_7$:Eu^{3+}NPs prepared with different coprecipitating pH values through experimental and theoretical studies. Inorganic Chemistry, 2018, 57: 11815–11830
161. Cao J, Chen L, Chen W, Xu D, Sun X, Guo H. Enhanced emissions in self-crystallized oxyfluoride scintillating glass ceramics containing KTb_2F_7 nanocrystals. Optical Materials Express, 2016, 6(7): 2201–2206
162. Schwartz K. Atomic Physics Methods in Modern Research. Berlin: Springer, 1997
163. Benitez E, Husk D, Schnatterly S, Tarrio C. A surface recombina-

tion model applied to large features in inorganic phosphor efficiency measurements in the soft X-ray region. Journal of Applied Physics, 1991, 70(6): 3256–3260

164. Mikhailik V, Kraus H, Miller G, Mykhaylyk M, Wahl D. Luminescence of $CaWO_4$, $CaMoO_4$, and $ZnWO_4$ scintillating crystals under different excitations. Journal of Applied Physics, 2005, 97(8): 083523
165. Sen S, Tyagi M, Sharma K, Sarkar P S, Sarkar S, Basak C B, Pitale S, Ghosh M, Gadkari S C. Organic-inorganic composite films based on $Gd_3Ga_3Al_2O_{12}$:Ce scintillator nanoparticles for X-ray imaging applications. ACS Applied Materials & Interfaces, 2017, 9(42): 37310–37320
166. Demkiv T, Halyatkin O, Vistovskyy V, Gektin A, Voloshinovskii A. Luminescent and kinetic properties of the polystyrene composites based on BaF_2 nanoparticles. Nuclear Instruments & Methods in Physics Research. Section A, Accelerators, Spectrometers, Detectors and Associated Equipment, 2016, 810: 1–5
167. Demkiv T, Halyatkin O, Vistovskyy V, Hevyk V, Yakibchuk P, Gektin A, Voloshinovskii A. X-ray excited luminescence of polystyrene composites loaded with SrF_2 nanoparticles. Nuclear Instruments & Methods in Physics Research. Section A, Accelerators, Spectrometers, Detectors and Associated Equipment, 2017, 847: 47–51
168. Martins P, Martins P, Correia V, Rocha J, Lanceros-Mendez S. Gd_2O_3:Eu nanoparticle-based poly (vinylidene fluoride) composites for indirect X-ray detection. Journal of Electronic Materials, 2015, 44(1): 129–135
169. Oliveira J, Martins P, Martins P, Correia V, Rocha J, Lanceros-Mendez S. Gd_2O_3:Eu^{3+}/PPO/POPOP/PS composites for digital imaging radiation detectors. Applied Physics A, Materials Science & Processing, 2015, 121(2): 581–587
170. Kang Z, Zhang Y, Menkara H, Wagner B K, Summers C J, Lawrence W, Nagarkar V. CdTe quantum dots and polymer nanocomposites for X-ray scintillation and imaging. Applied Physics Letters, 2011, 98(18): 181914
171. Lawrence W G, Thacker S, Palamakumbura S, Riley K J, Nagarkar V V. Quantum dot-organic polymer composite materials for radiation detection and imaging. IEEE Transactions on Nuclear Science, 2012, 59(1): 215–221
172. Chen S, Gaume R. Transparent bulk-size nanocomposites with high inorganic loading. Applied Physics Letters, 2015, 107(24): 241906
173. Chen H, Rogalski M M, Anker J N. Advances in functional X-ray imaging techniques and contrast agents. Physical Chemistry Chemical Physics, 2012, 14(39): 13469–13486
174. Vistovskyy V, Zhyshkovych A, Halyatkin O, Mitina N, Zaichenko A, Rodnyi P, Vasil'ev A, Gektin A, Voloshinovskii A. The luminescence of BaF_2 nanoparticles upon high-energy excitation. Journal of Applied Physics, 2014, 116(5): 054308
175. Laval M, Moszyński M, Allemand R, Cormoreche E, Guinet P, Odru R, Vacher J. Barium fluoride—inorganic scintillator for subnanosecond timing. Nuclear Instruments and Methods in Physics Research, 1983, 206(1–2): 169–176
176. Im H J, Saengkerdsub S, Stephan A C, Pawel M D, Holcomb D E, Dai S. Transparent solid-state lithiated neutron scintillators based on self-assembly of polystyrene-block-poly(ethylene oxide) copolymer architectures. Advanced Materials, 2004, 16(19): 1757–1761
177. Kesanli B, Hong K, Meyer K, Im H J, Dai S. Highly efficient solid-state neutron scintillators based on hybrid sol–gel nanocomposite materials. Applied Physics Letters, 2006, 89(21): 214104
178. deKrafft K E, Boyle W S, Burk L M, Zhou O Z, Lin W. Zr- and Hf-based nanoscale metal-organic frameworks as contrast agents for computed tomography. Journal of Materials Chemistry, 2012, 22 (35): 18139–18144
179. Doty F, Bauer C, Skulan A, Grant P, Allendorf M. Scintillating metal-organic frameworks: a new class of radiation detection materials. Advanced Materials, 2009, 21(1): 95–101
180. Perry J J IV, Feng P L, Meek S T, Leong K, Doty F P, Allendorf M D. Connecting structure with function in metal–organic frameworks to design novel photo- and radioluminescent materials. Journal of Materials Chemistry, 2012, 22(20): 10235–10248
181. Alexander P, Lacey A, Lyons L. Absorption and luminescence origins in anthracene crystals. Journal of Chemical Physics, 1961, 34(6): 2200–2201
182. Dekker A, Lipsett F. Fluorescent spectra of some organic solid solutions. Canadian Journal of Physics, 1952, 30(3): 165–173
183. Helfrich W, Lipsett F. Fluorescence and defect fluorescence of anthracene at 4.2° K. Journal of Chemical Physics, 1965, 43(12): 4368–4376
184. Hubbell J, Seltzer S. NIST standard reference database 126, Gaithersburg, MD: National Institute of Standards and Technology 1996
185. Vistovskyy V, Zhyshkovych A, Chornodolskyy Y M, Myagkota O, Gloskovskii A, Gektin A, Vasil'ev A, Rodnyi P, Voloshinovskii A. Self-trapped exciton and core-valence luminescence in BaF_2 nanoparticles. Journal of Applied Physics, 2013, 114(19): 194306
186. Vistovskyy V, Zhyshkovych A, Mitina N, Zaichenko A, Gektin A, Vasil'ev A, Voloshinovskii A. Relaxation of electronic excitations in CaF_2 nanoparticles. Journal of Applied Physics, 2012, 112(2): 024325
187. Malyy T, Vistovskyy V, Khapko Z, Pushak A, Mitina N, Zaichenko A, Gektin A, Voloshinovskii A. Recombination luminescence of LaPO4-Eu and $LaPO_4$-Pr nanoparticles. Journal of Applied Physics, 2013, 113(22): 224305
188. Vistovskyy V, Malyy T, Pushak A, Vas'Kiv A, Shapoval A, Mitina N, Gektin A, Zaichenko A, Voloshinovskii A. Luminescence and scintillation properties of $LuPO_4$-Ce nanoparticles. Journal of Luminescence, 2014, 145: 232–236
189. Bizarri G, Moses W W, Singh J, Vasil'Ev A, Williams R. An analytical model of nonproportional scintillator light yield in terms of recombination rates. Journal of Applied Physics, 2009, 105(4): 044507
190. Sudheendra L, Das G K, Li C, Stark D, Cena J, Cherry S, Kennedy I M. $NaGdF_4$:Eu^{3+} nanoparticles for enhanced X-ray excited optical imaging. Chemistry of Materials, 2014, 26(5): 1881–1888
191. Sengupta D, Miller S, Marton Z, Chin F, Nagarkar V, Pratx G. Bright Lu_2O_3:Eu thin-film scintillators for high-resolution radioluminescence microscopy. Advanced Healthcare Materials, 2015, 4(14): 2064–2070
192. Ikesue A, Aung Y L. Synthesis and performance of advanced ceramic lasers. Journal of the American Ceramic Society, 2006, 89

(6): 1936–1944

193. McCauley J W, Patel P, Chen M, Gilde G, Strassburger E, Paliwal B, Ramesh K, Dandekar D P. AlON: a brief history of its emergence and evolution. Journal of the European Ceramic Society, 2009, 29(2): 223–236
194. Cherepy N, Kuntz J, Seeley Z, Fisher S, Drury O, Sturm B, Hurst T, Sanner R, Roberts J, Payne S. Transparent ceramic scintillators for gamma spectroscopy and radiography. In: Proceedings of Hard X-Ray, Gamma-Ray, and Neutron Detector Physics XII, International Society for Optics and Photonics, 2010, 78050I
195. Kielty M W. Cerium doped glasses: search for a new scintillator. Dissertation for the Master Degree. Clemson: Clemson University, 2016
196. Biswas A, Maciel G, Friend C, Prasad P. Upconversion properties of a transparent Er^{3+}–Yb^{3+} co-doped LaF_3–SiO_2 glass-ceramics prepared by sol–gel method. Journal of Non-Crystalline Solids, 2003, 316(2–3): 393–397
197. de Faoite D, Hanlon L, Roberts O, Ulyanov A, McBreen S, Tobin I, Stanton K T. Development of glass-ceramic scintillators for gamma-ray astronomy, Journal of Physics: Conference Series, 2015, 012002
198. Barta M B, Nadler J H, Kang Z, Wagner B K, Rosson R, Kahn B. Effect of host glass matrix on structural and optical behavior of glass–ceramic nanocomposite scintillators. Optical Materials, 2013, 36(2): 287–293
199. Baccaro S, Cecilia A, Mihokova E, Nikl M, Nitsch K, Polato P, Zanella G, Zannoni R. Radiation damage induced by γ irradiation on Ce^{3+} doped phosphate and silicate scintillating glasses. Nuclear Instruments & Methods in Physics Research. Section A, Accelerators, Spectrometers, Detectors and Associated Equipment, 2002, 476(3): 785–789
200. Kang Z, Wagner B K, Nadler J H, Rosson R, Kahn B, Barta M B. Transparent glass scintillators, methods of making same and devices using same. Google Patents, 2016
201. Chen W, Cao J, Hu F, Wei R, Chen L, Sun X, Guo H. Highly efficient $Na_5Gd_9F_{32}$:Tb^{3+} glass ceramic as nanocomposite scintillator for X-ray imaging. Optical Materials Express, 2018, 8(1): 41–49
202. Hammig M D. Nanoscale Methods to Enhance the Detection of Ionizing Radiation. In: Nenoi M, ed. Current Topics in Ionizing Radiation Research. London: IntechOpen, 2012
203. Guss P, Guise R, Yuan D, Mukhopadhyay S, O'Brien R, Lowe D, Kang Z, Menkara H, Nagarkar V V. Lanthanum halide nanoparticle scintillators for nuclear radiation detection. Journal of Applied Physics, 2013, 113(6): 064303
204. Hall R G. Nanoscintillators for radiation detection. Dissertation for the Master Degree. Arlington: The University of Texas at Arlington, 2013
205. Brown S, Rondinone A J, Dai S. (ORNL), Oak Ridge, TN (United States), 2007
206. Schlomka J P, Roessl E, Dorscheid R, Dill S, Martens G, Istel T, Bäumer C, Herrmann C, Steadman R, Zeitler G, Livne A, Proksa R. Experimental feasibility of multi-energy photon-counting K-edge imaging in pre-clinical computed tomography. Physics in Medicine and Biology, 2008, 53(15): 4031–4047
207. Morgan N Y, Kramer-Marek G, Smith P D, Camphausen K, Capala J. Nanoscintillator conjugates as photodynamic therapy-based radiosensitizers: calculation of required physical parameters. Radiation Research, 2009, 171(2): 236–244
208. Chen H, Wang G D, Chuang Y J, Zhen Z, Chen X, Biddinger P, Hao Z, Liu F, Shen B, Pan Z, Xie J. Nanoscintillator-mediated X-ray inducible photodynamic therapy for *in vivo* cancer treatment. Nano Letters, 2015, 15(4): 2249–2256
209. Clement S, Deng W, Camilleri E, Wilson B C, Goldys E M. X-ray induced singlet oxygen generation by nanoparticle-photosensitizer conjugates for photodynamic therapy: determination of singlet oxygen quantum yield. Scientific Reports, 2016, 6(1): 19954
210. Yu X, Liu X, Wu W, Yang K, Mao R, Ahmad F, Chen X, Li W. CT/MRI-guided synergistic radiotherapy and X-ray inducible photodynamic therapy using Tb-doped Gd-W-nanoscintillators. Angewandte Chemie International Edition, 2019, 58(7): 2017–2022
211. Wang H, Lv B, Tang Z, Zhang M, Ge W, Liu Y, He X, Zhao K, Zheng X, He M, Bu W. Scintillator-based nanohybrids with sacrificial electron prodrug for enhanced X-ray-induced photodynamic therapy. Nano Letters, 2018, 18(9): 5768–5774
212. Bekah D, Cooper D, Kudinov K, Hill C, Seuntjens J, Bradforth S, Nadeau J. Synthesis and characterization of biologically stable, doped LaF_3 nanoparticles co-conjugated to PEG and photosensitizers. Journal of Photochemistry and Photobiology A: Chemistry, 2016, 329: 26–34
213. Butterworth K T, McMahon S J, Currell F J, Prise K M. Physical basis and biological mechanisms of gold nanoparticle radiosensitization. Nanoscale, 2012, 4(16): 4830–4838
214. Bulin A L, Truillet C, Chouikrat R, Lux F, Frochot C, Amans D, Ledoux G, Tillement O, Perriat P, Barberi-Heyob M, Dujardin C. X-ray-induced singlet oxygen activation with nanoscintillator-coupled porphyrins. Journal of Physical Chemistry C, 2013, 117 (41): 21583–21589
215. Moronne M M. Development of X-ray excitable luminescent probes for scanning X-ray microscopy. Ultramicroscopy, 1999, 77 (1–2): 23–36
216. Morgan N Y, Kramer-Marek G, Smith P D, Camphausen K, Capala J. Nanoscintillator conjugates as photodynamic therapy-based radiosensitizers: calculation of required physical parameters. Radiation Research, 2009, 171(2): 236–244
217. Liu B, Wen L, Zhao X. The structure and photocatalytic studies of N-doped TiO_2 films prepared by radio frequency reactive magnetron sputtering. Solar Energy Materials and Solar Cells, 2008, 92(1): 1–10
218. Chen W, Zhang J. Using nanoparticles to enable simultaneous radiation and photodynamic therapies for cancer treatment. Journal of Nanoscience and Nanotechnology, 2006, 6(4): 1159–1166
219. Chen W, Wang S, Westcott S, Zhang J. Energy-transfer nanocomposite materials and methods of making and using same. Google Patents, 2009
220. Pratx G, Carpenter C M, Sun C, Xing L. X-ray luminescence computed tomography via selective excitation: a feasibility study. IEEE Transactions on Medical Imaging, 2010, 29(12): 1992–1999
221. Pratx G, Carpenter C M, Sun C, Rao R P, Xing L. Tomographic molecular imaging of X-ray-excitable nanoparticles. Optics Letters, 2010, 35(20): 3345–3347

222. Li C, Di K, Bec J, Cherry S R. X-ray luminescence optical tomography imaging: experimental studies. Optics Letters, 2013, 38(13): 2339–2341
223. Welsher K, Liu Z, Sherlock S P, Robinson J T, Chen Z, Daranciang D, Dai H. A route to brightly fluorescent carbon nanotubes for near-infrared imaging in mice. Nature Nanotechnology, 2009, 4 (11): 773–780
224. Iverson N M, Barone P W, Shandell M, Trudel L J, Sen S, Sen F, Ivanov V, Atolia E, Farias E, McNicholas T P, Reuel N, Parry N M A, Wogan G N, Strano M S. *In vivo* biosensing via tissue-localizable near-infrared-fluorescent single-walled carbon nanotubes. Nature Nanotechnology, 2013, 8(11): 873–880
225. Yi H, Ghosh D, Ham M H, Qi J, Barone P W, Strano M S, Belcher A M. M13 phage-functionalized single-walled carbon nanotubes as nanoprobes for second near-infrared window fluorescence imaging of targeted tumors. Nano Letters, 2012, 12(3): 1176–1183
226. Rogach A L, Eychmüller A, Hickey S G, Kershaw S V. Infrared-emitting colloidal nanocrystals: synthesis, assembly, spectroscopy, and applications. Small, 2007, 3(4): 536–557
227. Naczynski D J, Sun C, Türkcan S, Jenkins C, Koh A L, Ikeda D, Pratx G, Xing L. X-ray-induced shortwave infrared biomedical imaging using rare-earth nanoprobes. Nano Letters, 2015, 15(1): 96–102
228. Naczynski D J, Tan M C, Zevon M, Wall B, Kohl J, Kulesa A, Chen S, Roth C M, Riman R E, Moghe P V. Rare-earth-doped biological composites as *in vivo* shortwave infrared reporters. Nature Communications, 2013, 4(1): 2199
229. Yorkston J. Recent developments in digital radiography detectors. Nuclear Instruments & Methods in Physics Research. Section A, Accelerators, Spectrometers, Detectors and Associated Equipment, 2007, 580(2): 974–985
230. Kim S, Park J, Kang S, Cha B, Cho S, Shin J, Son D, Nam S. Investigation of the imaging characteristics of the Gd_2O_3:Eu nanophosphor for high-resolution digital X-ray imaging system. Nuclear Instruments & Methods in Physics Research. Section A, Accelerators, Spectrometers, Detectors and Associated Equipment, 2007, 576(1): 70–74
231. Mupparapu M, Bhargava R N, Mullick S, Singer S R, Taskar N, Yekimov A. Development and application of a novel nanophosphor scintillator for a low-dose, high-resolution digital X-ray imaging system. International Congress Series, Elsevier, 2005, 1281: 1256–1261
232. Chen H, Patrick A L, Yang Z, VanDerveer D G, Anker J N. High-resolution chemical imaging through tissue with an X-ray scintillator sensor. Analytical Chemistry, 2011, 83(13): 5045–5049
233. Yu W W, Chang E, Drezek R, Colvin V L. Water-soluble quantum dots for biomedical applications. Biochemical and Biophysical Research Communications, 2006, 348(3): 781–786
234. Chen W. Nanoparticle fluorescence based technology for biological applications. Journal of Nanoscience and Nanotechnology, 2008, 8(3): 1019–1051
235. Chen W, Westcott S L, Wang S, Liu Y. Dose dependent X-ray luminescence in MgF_2:Eu^{2+}, Mn^{2+} phosphors. Journal of Applied Physics, 2008, 103(11): 113103
236. Liu Y, Zhang Y, Wang S, Pope C, Chen W. Optical behaviors of ZnO-porphyrin conjugates and their potential applications for cancer treatment. Applied Physics Letters, 2008, 92(14): 143901
237. Liu Y, Chen W, Wang S, Joly A G. Investigation of water-soluble X-ray luminescence nanoparticles for photodynamic activation. Applied Physics Letters, 2008, 92(4): 043901
238. Liu Y, Chen W, Wang S, Joly A G, Westcott S, Woo B K. X-ray luminescence of LaF_3:Tb^{3+} and LaF_3:Ce^{3+},Tb^{3+} water-soluble nanoparticles. Journal of Applied Physics, 2008, 103(6): 063105
239. Juzenas P, Chen W, Sun Y P, Coelho M A N, Generalov R, Generalova N, Christensen I L. Quantum dots and nanoparticles for photodynamic and radiation therapies of cancer. Advanced Drug Delivery Reviews, 2008, 60(15): 1600–1614
240. Klassen N V, Kedrov V V, Ossipyan Y A, Shmurak S Z, Shmyt'ko I M, Krivko O A, Kudrenko E A, Kurlov V N, Kobelev N P, Kiselev A P, Bozhko S I. Nanoscintillators for microscopic diagnostics of biological and medical objects and medical therapy. IEEE Transactions on Nanobioscience, 2009, 8(1): 20–32

Dr. **Santosh Kumar Gupta** is a Scientific Officer at the Radiochemistry Division, Bhabha Atomic Research Centre, since 2010. He received his B.Sc. degree from Delhi University, M.Sc. degree from the Indian Institute of Technology, Delhi, and Ph.D. degree from the Homi Bhabha National Institute, Mumbai, India. He has been awarded with various international fellowships, such as Indo-US, JSPS, and Fulbright for Postdoctoral studies. He was the recipient of the Department of Atomic Energy Group Achievement and Young Scientist award from the Govt. of India for 2010 and 2017, respectively. As of today, he has published 137 journal articles with approximately 2200 citations and an *h*-index of 28. His area of research encompasses photo/radioluminescence of lanthanide and actinides, defect spectroscopy, upconversion of nanoparticles, optical materials for health, energy and environment, etc.

Dr. **Yuanbing Mao** is a professor of Chemistry at Illinois Institute of Technology. He received his B.Sc. degree from Xiangtan University, M.Sc. degree from the Institute of Chemistry, Chinese Academy of Sciences, and Ph.D. degree from the State University of New York at Stony Brook. He has earned several awards, including the Department of Defense Young Investigator Award and the Outstanding Mentorship Award from the Council on Undergraduate Research, and is a recipient of the DOE Visiting Faculty Program. As of today, he has published more than 100 peer-reviewed journal articles as well as some book chapters and patents. His research interests include nanomaterials, solid-state science and nanoscience with expertise in optoelectronics, energy storage and conversion, and environmental remediation.